# Downlink Performance of Optical Attocell Networks

Cheng Chen, Student Member, IEEE, Dushyantha A. Basnayaka, Member, IEEE, and Harald Haas, Member, IEEE

(Tutorial Review)

Abstract—An optical attocell network is proposed as an indoor small-cell cellular network based on visible light communication. In this paper, the downlink performance of optical attocell networks is comprehensively analyzed. In particular, signal-to-interferenceplus-noise ratio, outage probability, and the resulting achievable cell data rates of optical attocell networks with optical orthogonal frequency division multiplexing are analyzed. With different lighting network designs, the cell deployments of optical attocell networks may vary considerably. Hence, attocell networks with different cell deployments are considered and compared. The results show that the hexagonal and Poisson point process random cell deployments represents the best- and the worst-case performance of practical optical attocell deployments, respectively. In addition, the performance of optical attocell networks is compared with that achieved by other radio frequency small-cell networks. The results show that a well-designed optical attocell network can perform better than the state-of-the-art femtocell network or millimeter-wave system in terms of indoor area data rate (data rate per unit area).

Index Terms—Cellular network, optical attocell network, orthogonal frequency division multiplexing (OFDM), Poisson point process (PPP), visible light communication (VLC).

#### I. INTRODUCTION

7 ITH the introduction of mobile communication technologies, the number of wireless data services and users have increased significantly. This has resulted in a considerable increase in wireless data traffic [1]. If this trend continues, the limited available radio frequency (RF) spectrum would no longer fulfill the future wireless data traffic demand. One of the solutions to this challenge is to explore the visible light region of the electromagnetic spectrum for wireless data communication. This is generally referred to as visible light communication (VLC) [2]. It has been recognized that wireless data mostly originates in indoor environments (70%) [3]. Therefore, using indoor luminaries for wireless data transmission offers a promising solution to alleviate the exponentially increasing traffic of existing RF wireless systems. In addition, VLC has advantages such as license-free bandwidth and secure data transmission. In addition, the visible light spectrum is 1000 times larger than the entire 300 GHz RF spectrum, and it use does not generate interference to existing RF systems [4].

Key techniques to enhance spectral efficiency of wireless communication systems include advanced transmission

Manuscript received June 29, 2015; revised November 15, 2015; accepted December 15, 2015. Date of publication December 21, 2015; date of current version January 24, 2016. The work of Professor H. Haas was supported by EPSRC under Established Career Fellowship Grant EP/K008757/1.

The authors are with the University of Edinburgh, Li-Fi Research and Development Centre, Edinburgh EH9 3JL U.K. (e-mail: cheng.chen@ed.ac.uk; d.basnayaka@ed.ac.uk; h.haas@ed.ac.uk).

Color versions of one or more of the figures in this paper are available online at http://ieeexplore.ieee.org.

Digital Object Identifier 10.1109/JLT.2015.2511015

schemes that harness the spatial dimension, channel aggregation, improved resource allocation, and cell densification. Among these techniques, cell densification has been shown to be the most effective approach, which can potentially achieve over 1000-fold area spectral efficiency (ASE) gains [3]. Therefore, the small-cell concept as part of heterogeneous wireless networks is a key enabling element. A femtocell network is one such indoor small-cell system. Research has shown that the femtocell system can significantly increase the ASE of a cellular system [5]. VLC enables a step-change improvement of the small-cell concept while completely avoiding interference to incumbent wireless networks [6]. Each light fixture in a room is used as an optical base station (BS) to serve multiple users. This VLC cellular network is termed an optical light fidelity (LiFi) attocell network. Similar to a femtocell network, an optical attocell exhibits full functionality offered by a cellular system (full duplexing, multiple access and handover). However, its cell size is smaller, and it uses the license-free visible light spectrum. With the development of solid state lighting technology, a light emitting diode (LED) is now commonly used by the lighting industry due to its high energy efficiency and long lifetime. Therefore, an LED is considered to be used as the main element of the transmitter side. Since an LED is a non-coherent light source, intensity modulation (IM) is the most appropriate method to encode digital information [7]. A photo-diode (PD) is used as the main element at the receiver side, which directly converts the received optical intensity into an electrical current signal. This mechanism is referred to as direct detection (DD).

One of the main factors that limits the maximum achievable data rate of an LED/PD based VLC system is the available modulation bandwidth, which is mainly limited by the response time of the front-end devices, primarily the LED device. Thus, research has been carried out to expand the bandwidth of the LED. In [8], a commercially available phosphor-based LED is considered. By filtering out the phosphor component of the optical output, a 3-dB bandwidth of 20 MHz can be achieved with only the blue component of the optical output. In [9], a single  $50-\mu m$ gallium nitride LED is used in an experimental VLC link. The measured channel 3 dB bandwidth is about 60 MHz. Modulation techniques that ensure non-negativity of the signal while achieving close to optimum practical data rates are developed [10]. In [11], two types of optical-orthogonal frequency division multiplexing (O-OFDM) are introduced, namely, DC (direct current)biased optical (DCO)-OFDM and asymmetrically clipped optical (ACO)-OFDM. In [10], [12], enhanced unipolar OFDM (eU-OFDM) is proposed. eU-OFDM combines the advantages of DCO-OFDM and ACO-OFDM in a unique way. This results in both excellent spectral and also energy efficiency. In an attempt to study the achievable data rate of a single link VLC, an adaptive DCO-OFDM/discrete multitone (DMT) transmission scheme is used in [9], [13], [14]. In particular, in [9], adaptive DCO-OFDM is combined with a large bandwidth  $\mu$ LED, and this system achieves a data rate of 3 Gb/s. One of the limiting factors for the performance of an optical attocell network is co-channel interference (CCI) caused by using the same transmission resources in adjacent cells. Therefore, several methods have been studied to mitigate CCI in optical attocell networks. In [15] and [16], the concept of fractional frequency reuse and joint transmission is introduced in an optical attocell network, respectively. The results show an improvement in terms of both signal quality and spectral efficiency. In addition, a busy-burst signaling approach is applied in an optical wireless system deployed in an aircraft cabin environment [17]. Spatial diversity is explored in an optical attocell system: in [18] and [19], an angular diversity receiver and spatial division multiple access are considered in an optical attocell network, respectively. Multiple-input multiple-output techniques are considered in VLC systems in [20]-[22]. In addition, the application of orbital angular momentum technique to optical wireless communication is studied in [23].

An optical attocell network is a newly proposed concept which has great potential. There is very little research on the performance of such systems. In [24], an analytical framework for the downlink of an optical attocell network with hexagonal (HEX) cell deployment is proposed. A semi-analytical approach was presented to calculate the statistics of the signal-to-interference-plus-noise ratio (SINR) and spectral efficiency. This work extends [24] by providing an in-depth analysis of the downlink performance of an optical attocell network.

## A. Main Contributions

The main contributions of this study are summarized as follows:

- A system level downlink framework based on DCO-OFDM is introduced. This framework considers several important issues related to the calculation of the SINR. These issues include the available output signal power, the channel characteristics and signal clipping.
- 2) The effects of varying key network system parameters on the performance are studied. These parameters include the cell radius and Lambertian emission order of the LED light source. This study also provides guidelines for appropriate configurations of these aforementioned parameters.
- 3) Analytical expressions for the SINR statistics with HEX/Poisson point process (PPP) random networks are derived. HEX cell deployment is considered to be the idealized cellular structure. In contrast, the PPP network model represents the worst case cellular deployment. The analysis of the system performance of both cell deployments provides useful insights in the performance of practical optical attocell networks.
- 4) The performance of optical attocell networks in terms of data rate and coverage probability is evaluated and compared to the performance achieved by other RF smallcell systems.

The remainder of this paper is organized as follows: the downlink transmission framework is introduced in Section II.

The effects of key parameters are presented in Section III. The statistics of SINR with different cell deployment is presented in Section IV. The cell data rate and the outage probability of an optical attocell system are analyzed in Section V. The simulation results with infinite network model is compared to those with a finite network deployed in a room in Section VI. The multi-path (MP) effect due to room surface reflections is taken into account. The performance of the optical attocell systems with different cell deployments is compared in Section VII, and the significance of each cell deployment is discussed. The performance of optical attocell networks are compared to those achieved by other small-cell networks in Section VIII. Finally, the conclusions are given in Section IX.

The following notations are used in this paper:  $(\cdot)^*$  is the complex conjugate operation;  $\otimes$  is the convolution operator;  $\mathbb{E}[\cdot]$  is the statistical expectation;  $\mathbb{P}[\cdot]$  is the statistical probability.

## II. DOWNLINK FRAMEWORK

This study focuses on evaluating the downlink capacity of an optical attocell network. Generally, most of the system metrics are based on the achievable SINR. Therefore, this paper develops a framework to analyse the SINR in the system. Handover is important in optical attocell systems. However, mobile users in indoor environments are generally static or moving slowly. Therefore, handover is outside the scope of this study. The costeffective back-haul network can be realized by using power line communication or ethernet—in particular, power-over-ethernet where the same connection powers the light and provides gigabit connectivity. Alternatively, a high throughput back-haul network can be realized by optical fiber connection with passive optical networking or point-to-point wireless millimeter-wave (mmWave) connection [25]. It is assumed these back-haul connections can provide enough data capacity and would not limit the performance of the optical attocell network. Since this study focuses on the performance of the access network, the effect of the back-haul network is outside the scope of this study. The uplink connection is typically achieved by using wavelength division duplexing with wireless infrared or RF transmission [26], [27]. An in-depth analysis of the uplink performance of a LiFi attocell network is subject to future studies. It has been shown that using VLC in the downlink can off-load a large portion of traffic from RF communication systems [26]. Since the spectrum used for the uplink (infrared or RF) is sufficiently distant from the visible light spectrum, there is negligible interference between the uplink and the downlink.

## A. O-OFDM Transmission

In this study, O-OFDM systems are considered. Since the main objective is to achieve high data rates, a spectrum efficient DCO-OFDM system is analyzed as a candidate system. However, the analysis also applies to other types of O-OFDM systems in a similar manner. The block diagram of the downlink system is shown in Fig. 1. For each OFDM frame, K quadrature amplitude modulation (QAM) symbols are fed into the modulator. Since the 0th and K/2th samples require no energy, this amount of energy is equally distributed to the remaining samples to ensure that the time-domain signal is normalized. Therefore, the

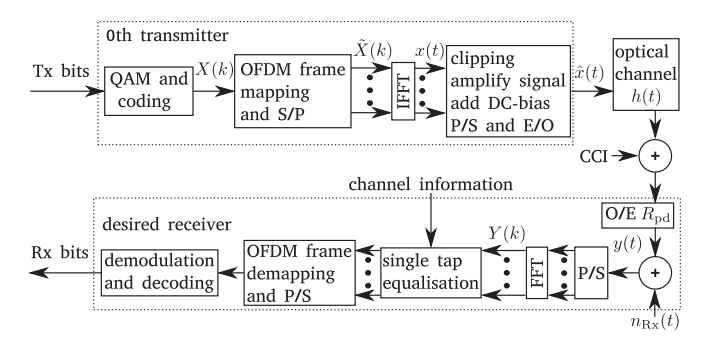


Fig. 1. An optical attocell network DCO-OFDM downlink system.

OFDM frame is normalized by a factor of  $\xi = \sqrt{K/(K-2)}$ . After the inverse fast Fourier transform (IFFT) operation, the real time domain signal x(t) follows a Gaussian distribution with zero mean and a unity variance. Next, a cyclic-prefix (CP) with a length based on the length of the maximum delay of the channel is added to the frame. Furthermore, the time domain signal x(t) is clipped, amplified by a factor of  $\sigma_x$  and biased by a DC component  $I_{\rm DC}$  in order to modulate the signal by the intensity of the light. The optical signal sample at time slot t can be written as:

$$\hat{x}(t) = \eta_{\text{led}} \left( \sigma_{\mathbf{x}} U(x(t)) + I_{\text{DC}} \right), \tag{1}$$

where  $\eta_{\rm led}$  denotes the electrical to optical conversion coefficient. Note that the output optical power is proportional to the input signal current;  $\sigma_x$  is equivalent to the standard deviation of the electrical signal; and the clipping function U(v) is defined as:

$$U(v) = \begin{cases} \lambda_{t} & : v > \lambda_{t} \\ v & : \lambda_{t} \ge v \ge \lambda_{b} \\ \lambda_{b} & : v < \lambda_{b} \end{cases}$$
 (2)

where  $\lambda_t$  and  $\lambda_b$  are the normalized top and bottom clipping levels, respectively [28]. According to the Bussgang theorem, the non-linear clipped signal can be modeled as follows:

$$U(x(t)) = \rho x(t) + n_{\text{clip}}(t), \tag{3}$$

where  $\rho$  is an attenuation factor and  $n_{\rm clip}(t)$  is the time domain clipping noise sample.

In this study, multiple optical BSs are considered. Among these BSs, the one offering the highest signal power is assigned to serve the desired user, and the BSs that use the same transmission resources within the remaining BSs causes CCI to the desired user. To distinguish the signals from different BSs, a subscript  $i=0,1,2,\ldots$  is added. The case of i=0 corresponds to the case of the desired BS, while  $i\in H$  corresponds to the case of the interfering BSs, in which H denotes the set of the BSs using the same transmission resources. Subsequently, the signals pass through the free-space optical channels and are received by the receiver of the desired user. The received signal sample at time slot t can be written as:

$$y(t) = \eta_{\rm pd} \left( \hat{x}_0(t) \otimes h_0(t) + \sum_{i \in \mathbf{M}} \hat{x}_i(t) \otimes h_i(t) \right) + n_{\rm Rx}(t),$$

$$(4)$$

where  $\eta_{\rm pd}$  is the PD responsivity of the receiver;  $h_i(t)$  denotes the channel impulse response of the VLC system from the ith BS to the desired user;  $n_{\rm Rx}(t)$  represents the time domain noise samples at the receiver. In conjunction with the clipping process modeling in (3), the frequency domain received signal sample on subcarrier k after the fast Fourier transform (FFT) operation can be written as:

$$Y(k) = \eta_{\rm pd} \eta_{\rm led} \sigma_{\rm x} \left( \rho X_0(k) + N_{\rm clip,0}(k) \right) H_0(k) + N_{\rm Rx}(k)$$
$$+ \eta_{\rm pd} \eta_{\rm led} \sigma_{\rm x} \sum_{i \in \mathcal{U}} \left( \rho X_i(k) + N_{\rm clip,i}(k) \right) H_i(k), \quad (5)$$

where  $H_i(k)$  is the frequency response of the VLC channel on the kth subcarrier;  $N_{\rm Rx}(k)$  corresponds to the frequency domain receiver noise which follows a Gaussian distribution with zero mean and variance of  $\sigma_{\rm Rx}^2$ . Here a noise power spectral density (PSD) of  $N_0$  is defined. With a sampling frequency (modulation bandwidth) of  $F_{\rm s}$ , the receiver noise variance  $\sigma_{\rm Rx}^2 = \frac{N_0 F_{\rm s}}{\xi^2}$ ; and  $N_{{\rm clip},i}(k)$  represents the FFT of  $n_{{\rm clip},i}(t)$ . According to the central limit theorem,  $N_{{\rm clip},i}(k)$  follows a Gaussian distribution with zero mean and a variance of  $\sigma_{{\rm clip}}^2$ . After the single-tap equalization, the desired signal can be recovered to the original QAM symbols  $X_0(k)$ , while the CCI is converted to Gaussian noise  $X_i(k)$  since the interfering signal is not synchronized with the desired user.

SINR is an important metric to evaluate the communication link quality and the transmission capacity in a cellular system. Based on (5), an expression for the SINR on subcarrier k can be written as:

$$\begin{split} \gamma(k) &= \left( \eta_{\rm pd}^2 \eta_{\rm led}^2 \sigma_{\rm x}^2 \rho^2 \xi^2 \left| H_0(k) \right|^2 \right) \! / \! \left( \eta_{\rm pd}^2 \eta_{\rm led}^2 \sigma_{\rm x}^2 \sigma_{\rm clip}^2 \left| H_0(k) \right|^2 \\ &+ \sum_{i \in \mathbf{M}} \eta_{\rm pd}^2 \eta_{\rm led}^2 \sigma_{\rm x}^2 \left( \rho^2 + \sigma_{\rm clip}^2 \right) \left| H_i(k) \right|^2 + \sigma_{\rm Rx}^2 \right) \\ &= \left( \left( \frac{\rho^2 \xi^2 \left| H_0(k) \right|^2}{\left( \rho^2 + \sigma_{\rm clip}^2 \right) \sum_{i \in \mathbf{M}} \left| H_i(k) \right|^2 + \frac{N_0 F_{\rm s}}{\xi^2 \eta_{\rm pd}^2 \eta_{\rm led}^2 \sigma_{\rm x}^2}} \right)^{-1} + \frac{\sigma_{\rm clip}^2}{\rho^2 \xi^2} \right)^{-1}, \end{split}$$
(6)

where the channel gain  $|H(k)|^2$ , the electrical signal variance  $\sigma_{\rm x}^2$ , the clipping related parameters  $\rho$ ,  $\sigma_{\rm clip}^2$  and the receiver noise PSD  $N_0$  are analyzed in the following sections. The general ways of calculating these terms are concluded.

#### B. Channel Model

As implied by formula (6), the VLC channel gain  $|H(k)|^2$  has an important role in the value of the SINR. The characteristics of  $|H(k)|^2$  is influenced by the response of the front-end devices (LED, PD) and of the free-space transmission. Therefore,  $|H(k)|^2$  can be modeled as:

$$|H(k)|^2 = |H_{fe}(k)|^2 |H_{fs}(k)|^2,$$
 (7)

where  $H_{\rm fe}(k)$  is the frequency response due to the filtering of the front-end device; and  $H_{\rm fs}(k)$  represents the frequency response accounting for the free-space transmission in an indoor environment.

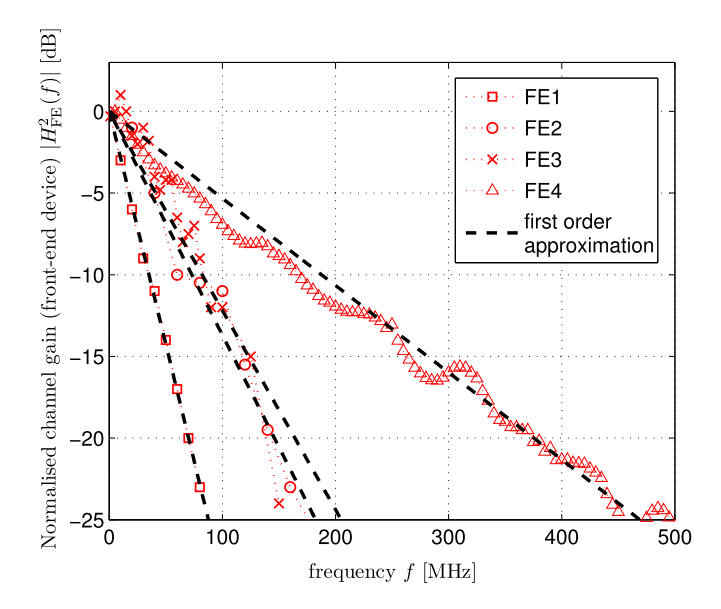


Fig. 2. Normalized channel gain due to the front-end device filtering. The channel gains of the FE1, FE2 and FE3 are presented in [8], [14], [13], respectively. Commercially available white LEDs are used in these systems. The channel gain of FE4 is an experimental measurement of the same system presented in [9] which uses a  $50-\mu m$  gallium nitride LED.

1) Front-End Device Filtering: The general effect of the front-end device filtering shows low-pass characteristics. The corresponding bandwidth is typically limited by the response speeds of the LED and the PD. Four normalized channel gains due to the front-end device filtering in [8], [14], [13] and [9] are demonstrated in Fig. 2. The 3-dB bandwidth of these systems are in the range from 10 to 60 MHz. Since the highest sampling frequency is about 1 GHz, this low-pass effect will significantly decrease the signal strength when using a high sampling rate. Therefore, the low-pass effect of the front-end device filtering is crucial to the performance of an optical attocell system.

However, it is trivial to characterize the exact front-end device property. The device property may vary with different specifications or even with different copies of the same specification. Therefore, a first order function is adopted to approximate the normalized channel gain of the front-end device filtering in this study as [8]:

$$|H_{\rm fe}(f)|^2 = \exp\left(-\frac{f}{F_{\rm fe}}\right),\tag{8}$$

where  $F_{\rm fe}$  controls the frequency characteristics of the front-end device. The higher the value of  $F_{\rm fe}$ , the wider the modulation bandwidth. As shown in Fig. 2, the approximations offer a good estimation of the low-pass characteristics. Converting (8) to the normalized channel gain on subcarrier k gives:

$$\left|H_{\rm fe}(k)\right|^2 = \exp\left(-\frac{kF_{\rm s}}{KF_{\rm fe}}\right),\tag{9}$$

for  $k=1,2,\ldots,K/2-1$ . In the remainder of this paper, systems with different front-end device are considered. For the convenience of description, the front-end device used in [8] is denoted as FE1 with a corresponding  $F_{\rm fe}$  of 15.2 MHz. Similarly, the front-end devices used in [14], [13] and [9] are denoted

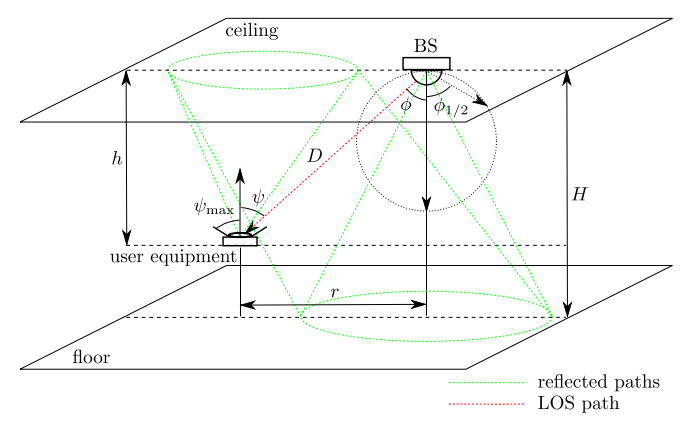


Fig. 3. Transmission geometry in an optical attocell system.

as FE2, FE3 and FE4 with corresponding  $F_{\rm fe}$  of 35.6, 31.7 and 81.5 MHz, respectively.

2) Free-Space Transmission: In this study, a geometric raytracing method is used to analyze the channel characteristics. The wireless transmission geometry is given in Fig. 3. The optical BS, oriented to the floor, is installed on the ceiling of the room. At the user side, the user receiver is placed at a certain height with the PD detector facing upward. This results in a vertical separation between user and the BS of h. The fixed direction of the PD detector can be achieved by using a mechanical design or by installing multiple PD detectors on the receiver. This is possible given the small size of PD detectors. Due to the limited space here, the effect of receiver rotation variance of vertical separation will be the subject of future research.

As shown in Fig. 3, the line-of-sight (LOS) path transmission between a pair of BS and user is considered here. This LOS path free-space transmission channel can be calculated using the DC channel gain  $H_{\rm los}$  between the BS and the desired user as [29]:

$$H_{\text{los}} = \frac{A_{\text{pd}}(m+1)}{2\pi D^2} \cos^m(\phi) \cos(\psi) \mathbf{1}_{\Lambda_1}(\psi), \qquad (10)$$

$$H_{\text{los}}(r) = \frac{A_{\text{pd}}(m+1)h^{m+1}\mathbf{1}_{\prod_{1}}(\psi)}{2\pi (r^{2} + h^{2})^{\frac{m+3}{2}}},$$
(11)

where m denotes the Lambertian emission order which is given by  $m=-\ln(2)/\ln(\cos(\phi_{1/2}))$  in which  $\phi_{1/2}$  is the half-power semi-angle of the LED. This quantity determines the beam width of the light source;  $A_{\rm pd}$  is the physical area of the receiver PD; D is the Euclidean distance between the BS and the user;  $\phi$  is the corresponding light radiance angle;  $\psi$  is the corresponding light incidence angle; and the function  $\mathbf{1}_{\Pi}(x)$  is defined as:

$$\mathbf{1}_{\mathbf{\Pi}}(x) = \begin{cases} 1 : x \in \mathbf{\Pi} \\ 0 : x \notin \mathbf{\Pi}. \end{cases}$$
 (12)

In (10),  $\Pi_1 = [0, \psi_{\text{max}}]$ , where  $\psi_{\text{max}}$  is the field of view (FOV) of the receiver. According to the geometry shown in Fig. 3,  $H_{\text{los}}$  can be rewritten as a function of the horizontal offset r between the BS and the user, as implied by (11).

As shown in Fig. 3, another source of the received signal is from the reflected paths, which mainly result from reflections

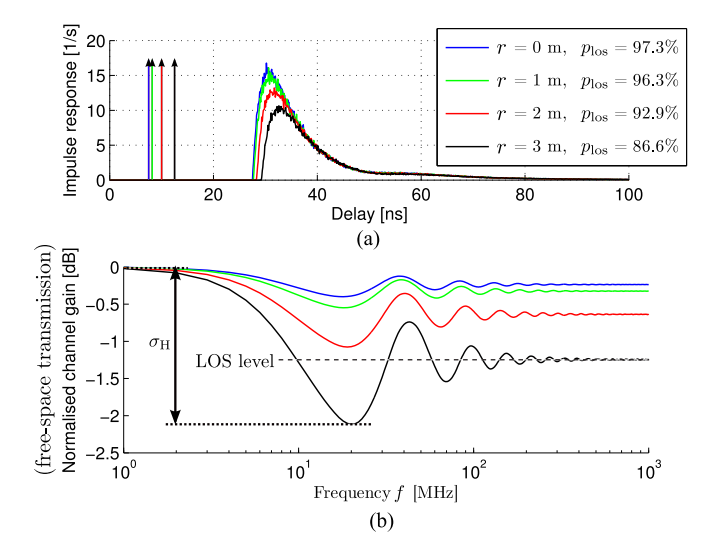


Fig. 4. (a) Channel impulse response in time domain. (b) Normalized channel gain in frequency domain.

by the room internal surfaces (walls, ceiling and floor). Diffuse reflections are considered in this study as typically these internal surfaces have a rough surface campared to the considered wavelengths. A large room with edge length of 5 m to 50 m is considered to accommodate the multi-cell VLC system. In this case, most of the users and BSs are away from the room edges. Consequently, in most cases (in the cells not near walls) the signal contribution from the first order reflection would be negligible. Therefore, the MP effect is mainly caused by the second order reflections bounced by the floor and ceiling.

In order to evaluate the effect of the reflected signals on the channel, computer simulations based on [30] are carried out. To simplify the problem, an extreme case is simulated with the floor and ceiling extending infinitely in all directions. A pair of serving BS and user is considered with a horizontal offset of r. The transmission geometry is given in Fig. 3. The simulation time bin width is 0.1 ns and the number of iterations is  $5\times10^5$ . The results of four example channels with r=0,1,2,3 m are shown in Fig. 4 in the form of the time domain impulse response and the frequency domain normalized channel gain. A dispersive source with  $\phi_{1/2}$  of  $60^\circ$  is simulated. The reflectivity of the ceiling is 0.7 and the reflectivity of the floor is 0.3. The height of the room is 3 m and the measured plane is 0.75 m above the floor.

In Fig. 4(a), the impulse response results show that the first received signal is a strong LOS component, followed by a period of no signals until the first reflected signal reaches the receiver. Then, it is followed by a stream of closely spaced reflected signals. This is because the signal propagation delay of the LOS path is much shorter than the delay incurred by the reflected paths. To show the strength of the LOS component, a parameter  $p_{\rm los}$  is defined.  $p_{\rm los}$  represents the ratio of the received optical power of the LOS signal component to the total received optical power. These channels result in normalized channel gains  $\left|\frac{H_{\rm fs}(f)}{H_{\rm fs}(0)}\right|^2$  as shown in Fig. 4(b). The maximum channel gain always appears at DC. With an increase of frequency, the channel gain decreases and reaches a minimum value at about 20 MHz. With a further increase of the frequency, the channel gain

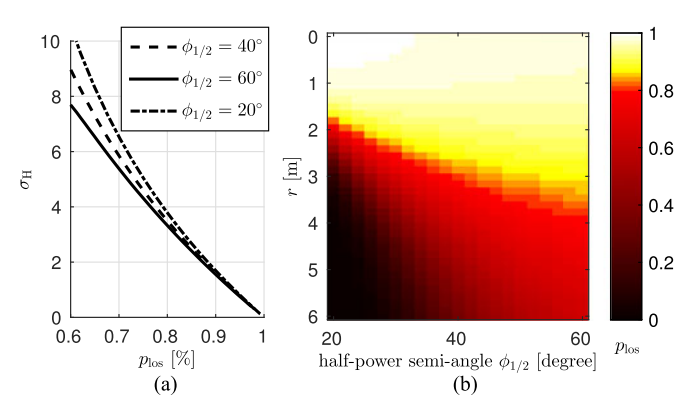


Fig. 5. (a) Maximum channel gain variance  $\sigma_{\rm H}$  against power proportion of LOS component  $p_{\rm los}$ . (b)  $p_{\rm los}$  against transmission horizontal offset  $r_0$  and half-power semi-angle  $\phi_{1/2}$ .

oscillates at a constant level and the magnitude of this oscillation diminishes. The constant level corresponds to the channel gain considering the LOS component only. It can be observed that the maximum variance in the channel gain  $\sigma_{\rm H}$  is less than 2.5 dB. This means that the variation of the channel gain due to the reflected signal is minor compared to the effect due to the limitation of the front-end device filtering.

It is known that the flatness of the channel gain is strongly related to the strength of the LOS component [31]. Therefore, the relationship between the maximum channel gain variance  $\sigma_{\rm H}$  and the proportion of the LOS power  $p_{\rm los}$  is evaluated using simulation with different transmitter half-power semi-angles  $\phi_{1/2}$ . It can be observed that  $\sigma_{\rm H}$  is a decreasing function of  $p_{\rm los}$ , as shown in Fig. 5(a). As long as  $p_{\rm los}$  is above 80%,  $\sigma_{\rm H}$  can be kept below 4 dB. Instead of evaluating the channel gain directly,  $p_{\rm los}$  can be evaluated to estimate the flatness of the channel gain. In addition to the case shown in Fig. 4, the performance with all of the configurations of interest needs to be considered. Specifically,  $p_{\rm los}$  is evaluated using different r and  $\phi_{1/2}$ . In conjunction with the analysis in Section III, it is shown that in this study,  $p_{los}$ is always high in the region of interest as shown in Fig. 5(b). This is due to the longer traveling distance  $\ell$  in combination with the high electrical path loss in IM/DD systems,  $L \propto (\ell)^4$ , and the high absorption by the floor and ceiling.

The results shown in Figs. 4 and 5 do not cover the performance of users near the edge of the room. Therefore,  $p_{los}$ considering reflections from all surfaces of a room is calculated in an example room, in order to validate the assumption that the first order reflection is negligible in most cases. In this example, 23 HEX cells in a room of size of 26 m  $\times$  26 m  $\times$  3 m are considered. A half-power semi-angle  $\phi_{1/2}$  of  $60^{\circ}$ , and cell radius R of 3 m are used. The result is shown in Fig. 6(a). Users in the cells not close to the room edges have  $p_{los}$  above 85%. In addition, users in the center of the room edge cells also have high  $p_{los}$ . The remaining users in the cells close to the walls have a lower value of  $p_{los}$ , but generally above 50%. The results given in Fig. 6(a) are also presented in the form of the cumulative distribution function (CDF), shown as the setup 1 curve in Fig. 6(b). Fig. 6(b) shows that nearly 80% of the users experience  $p_{\rm los}$  above 80%. Although the indoor signal propagation causes

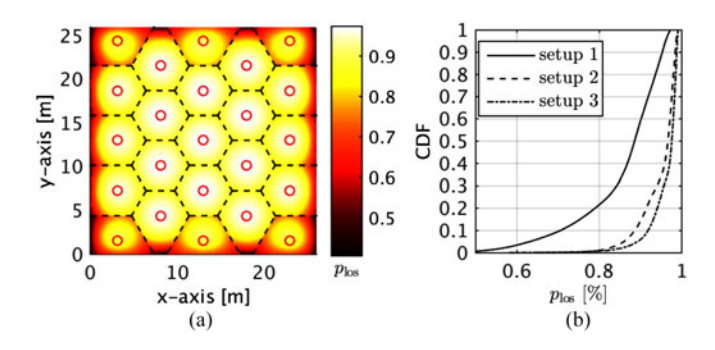


Fig. 6. (a) Spatial distribution of  $p_{\rm los}$  in setup 1:  $\phi_{1/2}=60^\circ$ ,  $R=3\,$  m,  $L_{\rm room}=26\,$ m. (b)  $p_{\rm los}$  distribution in the form of CDF. Setup 2:  $\phi_{1/2}=20^\circ$ ,  $R=1\,$ m,  $L_{\rm room}=8.5\,$ m. Setup 3:  $\phi_{1/2}=20^\circ$ ,  $R=1\,$ m,  $L_{\rm room}=14.5\,$ m.

some considerable frequency selectivity in the channel for the remaining 20% of the low  $p_{\rm los}$  users, the inter-symbol interference can be easily removed by the use of OFDM in conjunction with a well-designed CP. In addition, the  $p_{\rm los}$  distribution with smaller  $\phi_{1/2}$  of  $20^\circ$  and R=1 m is demonstrated. When the number of cells is the same as the  $\phi_{1/2}=60^\circ$  case (setup 2), the room size is decreased to  $8.5~{\rm m}\times 8.5~{\rm m}\times 3~{\rm m}$ . The resulting  $p_{\rm los}$  CDF shows that about 99% of the users have  $p_{\rm los}$  above 80%. If the room size is increased to  $14.5~{\rm m}\times 14.5~{\rm m}\times 3~{\rm m}$  with  $67~{\rm cells}$  (setup 3),  $p_{\rm los}$  is further improved. Therefore, it can be concluded that the reflected signal causes negligible MP effect on the channel for the majority of the users as long as the user experiences a dominant LOS signal component. Thus,  $|H_{\rm fs}(k)| \approx H_{\rm los}$  for any k.

Occasionally, the LOS path may be shadowed or completely blocked. In these cases, a user may need an alternative serving BS or a diffused link.

## C. Light Source Output Power

The relationship between the electrical signal standard deviation  $\sigma_x$  and the output optical power  $P_{\rm opt}$  from the light source can be written as [28]:

$$P_{\text{opt}} = \mathbb{E}\left[\hat{x}(t)\right] = \eta_{\text{led}}\left(\sigma_{\mathbf{x}}\mathbb{E}\left[U(x(t))\right] + I_{\text{DC}}\right). \tag{13}$$

Generally, a fixed ratio of DC-bias level to the electrical signal standard deviation is defined as  $\zeta = \frac{I_{\rm DC}}{\sigma_{\rm x}}$ . By combining (13) with  $\zeta$ , it can be found that:

$$\sigma_{\mathbf{x}}^{2} = \frac{P_{\text{opt}}^{2}}{\eta_{\text{led}}^{2} \left(\zeta + \mathbb{E}\left[U(x(t))\right]\right)^{2}},\tag{14}$$

which represents the maximum possible  $\sigma_{\rm x}^2$  with a given  $P_{\rm opt}$ . To get more electrical signal power, more optical power is needed assuming that the denominator in (14) is constant. However, optical power is finite and is typically constrained by the illumination requirement. This requirement is specified by the indoor lighting regulation [32], which requires a maintained illuminance of 500 lux in a typical working indoor environment for writing and reading purposes. To accommodate this requirement, the illuminance in the area below the luminary (cell center) should be at least 500 lux. According to the analysis in Section II-B2, the illuminance at the cell center can be

calculated as:

$$E_{\rm v} = \Phi_{\rm v} \frac{H_{\rm los}(0)}{A_{\rm pd}} = \frac{(m+1)\Phi_{\rm v}}{2\pi h^2},$$
 (15)

where  $\Phi_v$  is the output luminous flux of the luminary. It is the output power measure in photometry which corresponds to the optical power in radiometry [33]. The conversion between luminous flux and radiant optical power can be given as:

$$\frac{\Phi_{\rm v}}{P_{\rm opt}} = K_{\rm e/v} = \frac{683 \int V(\lambda) \Phi_{\rm e}(\lambda) d\lambda}{\int \Phi_{\rm e}(\lambda) d\lambda},$$
 (16)

where  $K_{\rm e/v}$  is called luminous efficacy;  $V(\lambda)$  is the luminosity function against wavelength  $\lambda$ ; and  $\Phi_{\rm e}(\lambda)$  is the spectral radiant power density function. The value of  $K_{\rm e/v}$  is determined by the characteristic of the specific LED chip in the system. Therefore, the configuration of  $P_{\rm opt}$  can be calculated as:

$$P_{\text{opt}} = \frac{\Phi_{\text{v}}}{K_{\text{e/v}}} = \frac{2\pi E_{\text{v}} h^2}{(m+1)K_{\text{e/v}}}.$$
 (17)

Considering a room height of 3 m, with a  $\phi_{1/2}$  of  $20^\circ$  to  $45^\circ$ , the required luminous flux for a minimum illuminance of 500 lux is in the range of 1300 to 5300 lumen. This amount of power agrees with the specification of commercially available LED downlighters and LED panels for lighting in offices and public areas [34], [35]. Note that the LED lamp output level for residential home is typically lower than this level (< 1000 lumen). However, this does not necessarily affect the communication performance as only a fraction of the optical output power, modelled by  $\zeta$ , is used for the communication link. Moreover, by closer inspection of (3) and (14) it can be found that the performance also depends on the signal clipping, i.e., the linearity of the LED transfer characteristic. An optimization of these parameters is beyond the scope of this work, and the interested reader is referred to [7].

#### D. Signal Clipping

In this study, the results in [28] are used to calculate the effects caused by the signal clipping process in (1). First, clipping affects the transfer relationship between BS output optical power and electrical signal power as shown in (14). The expectation of the clipped signal  $\mathbb{E}\left[U(x(t))\right]$  in (14) can be calculated by [28]:

$$\mathbb{E}\left[U(x(t))\right] = \left(f_{\mathcal{N}}(\lambda_{\mathrm{b}}) - f_{\mathcal{N}}(\lambda_{\mathrm{t}}) + \lambda_{\mathrm{t}} \mathcal{Q}(\lambda_{\mathrm{t}}) + \lambda_{\mathrm{b}} (1 - \mathcal{Q}(\lambda_{\mathrm{b}}))\right) \tag{18}$$

where  $\mathcal{Q}(u)=\frac{1}{\sqrt{2\pi}}\int_u^\infty \exp\left(-\frac{v^2}{2}\right)\mathrm{d}v$  is the Q-function; and  $f_{\mathcal{N}}(u)=\frac{1}{\sqrt{2\pi}}\exp\left(-\frac{u^2}{2}\right)$  is the probability density function (PDF) of the unit normal distribution. In addition, the transmitted signal is attenuated by a factor of  $\rho$  which can be calculated as  $\rho=\mathcal{Q}(\lambda_{\rm b})-\mathcal{Q}(\lambda_{\rm t})$ . Finally, the clipping noise variance  $\sigma_{\rm clip}^2$  can calculated as:

$$\sigma_{\text{clip}}^{2} = \mathcal{Q}(\lambda_{\text{b}}) - \mathcal{Q}(\lambda_{\text{t}}) + f_{\mathcal{N}}(\lambda_{\text{b}})\lambda_{\text{b}} - f_{\mathcal{N}}(\lambda_{\text{t}})\lambda_{\text{t}}$$

$$+ (1 - \mathcal{Q}(\lambda_{\text{b}}))\lambda_{\text{b}}^{2} + \mathcal{Q}(\lambda_{\text{t}})\lambda_{\text{t}}^{2} - \rho^{2}$$

$$- (f_{\mathcal{N}}(\lambda_{\text{b}}) - f_{\mathcal{N}}(\lambda_{\text{t}}) + (1 - \mathcal{Q}(\lambda_{\text{b}}))\lambda_{\text{b}} + \mathcal{Q}(\lambda_{\text{t}})\lambda_{\text{t}})^{2}.$$

$$(19)$$

#### E. Noise at Receiver

Three noise sources at the receiver side is considered in this study. The considered noise PSD  $N_0$  can be calculated as:

$$N_0 = N_{0,s} + N_{0,ab} + N_{0,th}, (20)$$

where  $N_{0,\rm s}$  corresponds to the shot noise caused by the received optical signal from the BS;  $N_{0,\rm ab}$  corresponds to the shot noise caused by the received ambient light (mainly daylight); and  $N_{0,\rm th}$  corresponds to the thermal noise in the receiver circuit. The PSD of the shot noise caused by the signal can be calculated as [29]:

$$N_{0,s} = 2q P_{\text{opt,Rx}} \eta_{\text{pd}}, \tag{21}$$

where q is the charge of an electron,  $1.6 \times 10^{-19}$  C;  $P_{\rm opt,Rx}$  denotes the incident optical power to the PD detector at the receiver from the optical BS. Intuitively, the main contributor of this amount of optical power is from the desired BS. To avoid unnecessary calculation complexity, the incident optical power from the remaining BSs is omitted. Thus,  $P_{\rm opt,Rx} = P_{\rm opt} H_{\rm los}(r_0)$ , where  $r_0$  denotes the horizontal offset between the desired BS and the considered user. The PSD of the shot noise caused by the ambient light can be calculated as [29]:

$$N_{0,ab} = 2qE_{r,ab}A_{pd}\eta_{pd}, \qquad (22)$$

where  $E_{\rm r,ab}$  denotes the incident irradiance in the indoor environment. Note that the actual effect of ambient light will be smaller as only the light with the signal spectrum causes distortion as long as an appropriate optical filter is used. Finally, the PSD of the thermal noise can be calculated as [17]:

$$N_{0,\text{th}} = \frac{4\mathcal{K}_{\rm B}T}{R_{\rm L}},\tag{23}$$

where  $\mathcal{K}_{\rm B}$  denotes the Boltzmann's constant with a value of  $1.38 \times 10^{-23}$  J/K; T denotes the absolute temperature; and  $R_{\rm L}$  denotes the load resistance in the receiver circuit.

$$\gamma(k) = \left( \frac{\rho^{2} \xi^{2} (r_{0}^{2} + h^{2})^{-m-3} \mathbf{1}_{\underline{\Pi}_{2}}(r_{0})}{\left(\rho^{2} + \sigma_{\text{clip}}^{2}\right) \sum_{i \in \underline{\mathbf{H}}} (r_{i}^{2} + h^{2})^{-m-3} \mathbf{1}_{\underline{\Pi}_{2}}(r_{i}) + \mathcal{Z}(k)} \right)^{-1} + \frac{\sigma_{\text{clip}}^{2}}{\rho^{2} \xi^{2}} \right)^{-1}$$

$$(24)$$

By inserting (7), (9), (11), (14) and (17) into the SINR expression (6), (6) can be modified as (24), where  $\Pi_2 = \left[0, h\sqrt{\sec^2(\psi_{\text{max}}) - 1}\right]$  and:

$$\mathcal{Z}(k) = \frac{K_{\text{e/v}}^2 N_0(r_0) F_{\text{s}} \exp\left(\frac{kF_{\text{s}}}{KF_{\text{fe}}}\right) \left(\zeta + \mathbb{E}\left[U(x(t))\right]\right)^2}{\left(\xi E_{\text{v}} A_{\text{pd}} \eta_{\text{pd}} h^{m+3}\right)^2}.$$
(25)

Note that  $N_0$  is a function of  $r_0$  as the shot noise varies with user locations with different received signal strength.

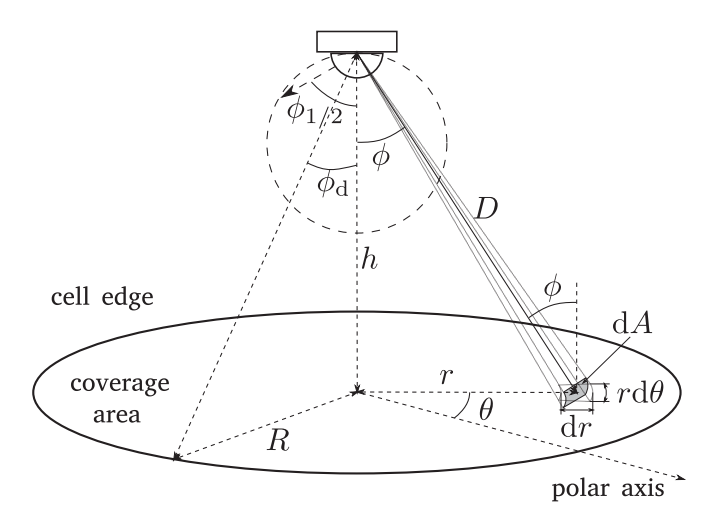


Fig. 7. Optical BS radiation geometry.

## F. Multiple-Access and Spatial Reuse Schemes

Since it is recognized that the channel magnitude response is mainly affected by the front-end device, the magnitude response excluding the path loss changes little with the location of the user. In other words, there is little multi-user diversity and therefore time-division is assumed to be used to separate the multiple users within a cell. In addition, in the system with reuse factor  $\Delta$  larger than 1, the resources are also divided in the frequency domain.

## III. SYSTEM PARAMETERS EVALUATION

The performance of an optical attocell network depends on many factors as implied by (24). Some of the parameters can be controlled by a predefined system configuration. In this section, two key parameters closely related to the network configuration are studied. One of the parameters is the cell radius R or BS density  $\Lambda$  of a network. These determine the number of users per cell and the number of cells in a room. The other parameter is the radiation pattern of the source, which is controlled by the Lambertian emission order, m. The pattern determines the signal strength distribution within each cell and the level of CCI to other cells. Appropriate configuration of these two parameters offers higher probability of achieving the desired system performance. Two configuration objectives are considered which include the maximization of desired signal strength and the minimization of introduced CCI.

#### A. CCI Minimization

In this section, a mathematical analysis is used to determine the appropriate setting for R and m with the objective of CCI minimization. Considering an optical BS with an optical output of  $P_{\rm opt}$  serving a cell underneath it, part of the radiated signal power falls within the desired coverage area, while the remaining signal power is incident on other cells as CCI. Fig. 7 shows the geometry of this setup. The considered BS is h away from the cell center. In order to minimize CCI, it is preferred to

allow more radiated signal power from the BS to stay within the coverage area of that BS, and to let less signal power leak into other cells. If the optical power reaching the desired coverage area is defined as  $P_{\rm opt,d}$ , the objective becomes maximizing  $P_{\rm opt,d}$ . First, the calculation of  $P_{\rm opt,d}$  should be determined. By considering the BS as the origin, the circular coverage area of the cell corresponds to a certain solid angle. Then, the desired signal power  $P_{\rm opt,d}$  for a certain solid angle can be calculated as [36]:

$$P_{\rm opt,d} = \int_{\rm cell} P_{\rm opt} \frac{m+1}{2\pi} \cos^m(\phi) d\Omega, \qquad (26)$$

where  $\Omega$  represents the solid angle of the radiation. The differential of this solid angle  $d\Omega$  can be derived as (27) according to the geometry shown in Fig. 7.

$$d\Omega = \frac{dA}{D^2} = \frac{r d\theta dr \cos(\phi)}{h^2 \sec^2(\phi)} = d\theta d\phi \sin(\phi).$$
 (27)

By inserting (27) into (26), the two-dimensional (2-D) integration can be decomposed into two one-dimensional integration as:

$$P_{\text{opt,d}} = P_{\text{opt}} \frac{m+1}{2\pi} \int_0^{2\pi} \int_0^{\phi_d} \cos^m(\phi) \sin(\phi) d\phi d\theta$$
$$= P_{\text{opt}} \left( 1 - \left( \frac{h}{\sqrt{h^2 + R^2}} \right)^{m+1} \right)$$
(28)

where  $\phi_{\rm d}$  can be calculated by  $\phi_{\rm d}=\arctan(R/h)$  as shown in Fig. 7. The partial derivatives of  $\phi_{\rm d}$  with respect to R and m are calculated as:

$$\frac{\partial P_{\text{opt,d}}}{\partial R} = \frac{P_{\text{opt}} R(m+1) h^{m+1}}{(h^2 + R^2)^{\frac{m+3}{2}}} > 0, \tag{29}$$

$$\frac{\partial P_{\text{opt,d}}}{\partial m} = P_{\text{opt}} \ln \left( \frac{\sqrt{h^2 + R^2}}{h} \right) \left( \frac{h}{\sqrt{h^2 + R^2}} \right)^{m+1} > 0, \quad (30)$$

which implies that  $P_{\rm opt,d}$  is a monotonically increasing function of R and m. This means that less CCI can be achieved by using a larger cell size as a larger cell size will increase the distance between each neighboring interfering BS and the desired user. In addition, using a source with a narrower beam width would also decrease the level of CCI as smaller half-power semi-angle leads to a more collimated beam pointing to the desired coverage area.

## B. Desired Signal Strength Maximization

Since the Lambertian radiation pattern is used to model the light emission from the source, the further the user is away from the cell center, the weaker the received desired signal. Consequently, the user at the cell edge receives the weakest signal from the BS. In other words, as long as the signal strength of the cell edge user is high enough, all of the users in the cell coverage area should have sufficient signal power. Therefore, the objective can be converted to maximizing the signal power received by the cell edge user who is R away from the cell center. According to the analysis in Section II-B2,  $P_{\rm opt,e}$  can be

determined as:

$$P_{\text{opt,e}} = P_{\text{opt}} H_{\text{los}}(R) = \frac{P_{\text{opt}} A_{\text{pd}}(m+1) h^{m+1}}{2\pi \left(R^2 + h^2\right)^{\frac{m+3}{2}}}.$$
 (31)

Similarly, the partial derivatives of  $P_{\rm opt,e}$  respect to R and m are calculated as:

$$\frac{\partial P_{\text{opt,e}}}{\partial R} = -\frac{P_{\text{opt}} A_{\text{pd}}(m+1)(m+3)Rh^{m+1}}{2\pi \left(R^2 + h^2\right)^{\frac{m+5}{2}}} < 0, \quad (32)$$

$$\frac{\partial P_{\text{opt,e}}}{\partial m} = \frac{P_{\text{opt}} A_{\text{pd}} h^{m+3} \left( 1 + \ln \left( \frac{h^{m+1}}{(R^2 + h^2)^{\frac{m+1}{2}}} \right) \right)}{2\pi h^2 \left( R^2 + h^2 \right)^{\frac{m+3}{2}}}.$$
 (33)

which implies that  $P_{\mathrm{opt,e}}$  is a monotonically decreasing function of R. Therefore, for a source with a specified radiation pattern, a smaller cell offers higher received signal power for the cell edge users. This is because a smaller cell size reduces the distance from the cell edge user to the cell center. On the other hand,  $P_{\mathrm{opt,e}}$  is a concave function of m, which means there is an optimal value for m to maximize the cell edge user signal strength. By letting  $\frac{\partial P_{\mathrm{opt,e}}}{\partial m}=0$ , the optimal radiation pattern can be calculated as:

$$\tilde{m} = 1/\ln\left(\sqrt{R^2 + h^2}/h\right) - 1.$$
 (34)

For the case of using a source with narrower beam width  $(m>\tilde{m})$ , the beam is over concentrated, which causes significant signal strength variance between cell center users and cell edge users, and the signal strength for the cell edge user would be too weak for reliable communication. For the case of using a source with wider beam width  $(m<\tilde{m})$ , the beam is over-diffused, which causes too much power leakage to other cells and the overall signal strength in the desired cell is not sufficient.

## C. Parameter Configurations

From the analysis in Sections III-A and B, it can be found that appropriate settings for R and m also is mutually dependant. Therefore, the configurations of cell size and source beam width should be interconnected. Apart from the requirement of communication, there are many other constraints on the configuration of cell size. For example, if the cell size is too large, the illumination performance will be undesired. An extremely small cell size leads to too many required BSs in the room, which increases the installation complexity and increases the load of the handover process. In contrast, beam width of the source is more flexible, which can be simply achieved by appropriate optical diffuser design. Therefore, the configuration of R is considered as a given parameter, and the suitable setting of m is analyzed.

According to (30) and (34), if m is smaller than  $\tilde{m}$ , CCI increases and cell edge signal strength decreases. If m is equal or greater than  $\tilde{m}$ , there is a trade-off between the two objectives. Therefore,  $\tilde{m}$  can be considered as a lower bound for m. In a noise limited system, a m closer to  $\tilde{m}$  is preferred. In the case of a CCI limited system, (30) shows that m should be maximized to minimize CCI. However, an upper bound should be set to allow the cell edge user signal strength to be high enough to

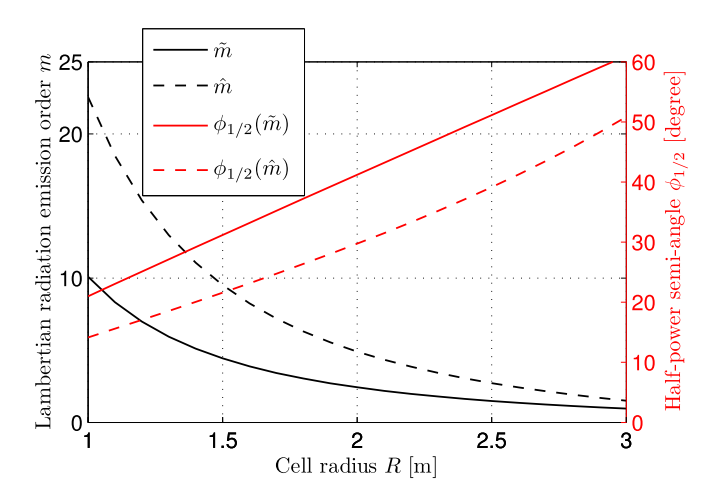


Fig. 8. The configuration of half-power semi-angle  $\phi_{1/2}$  and the corresponding Lambertian emission order m against the cell radius R.

achieve the minimum acceptable signal-to-noise ratio (SNR). In order to find this upper bound, a simple metric is defined: the ratio between the SNR of the cell center user (r=0) to that of the cell edge user (r=R), which is denoted as  $\sigma_{\rm P}$ . From the analysis in Section II, it can be deduced that  $\sigma_{\rm P}$  is proportional to the square of the ratio of received optical power by the cell center user to that received by the cell edge user as:

$$\sigma_{\rm P} = \left(\frac{P_{\rm opt} H_{\rm los}(0)}{P_{\rm opt} H_{\rm los}(R)}\right)^2 = \frac{h^{-2(m+3)}}{(R^2 + h^2)^{-m-3}}.$$
 (35)

For a fixed  $\sigma_{\rm P}$ , the required lower bound for m can be calculated as:

$$\hat{m} = \frac{\ln \sigma_{\rm P}}{\ln \left(1 + \frac{R^2}{h^2}\right)} - 3. \tag{36}$$

According to [9] and [13], the achievable cell center SNR is around 30 dB. For uncoded 4 QAM, the minimum required SNR is approximately 10 dB. Therefore,  $\sigma_{\rm P}=20$  dB is chosen in this study. The result of  $\tilde{m}$ ,  $\hat{m}$  and the corresponding  $\phi_{1/2}$  against R based on (34) and (36) are plotted in Fig. 8. It can be seen that the area between the two curves is the appropriate configuration region, which is the preferred settings for  $\phi_{1/2}$ . In the case that CCI is the main limiting factor, m can be set to a value that is close or equal to  $\hat{m}$ , which is calculated using (36). In the case that receiver noise is the limiting factor, m can be configured to a value that is close or equal to  $\tilde{m}$ , which is calculated using (34).

#### IV. SINR STATISTICS EVALUATIONS

The probability of receiving a certain service quality level can be determined by calculating the statistics of the achievable SINR. This metric is important as it directly determines the performance of an optical attocell network, such as achievable data rate and outage probability. The SINR statistics vary with large number of parameters, as noted in Sections II and III. In addition, it also varies with different cell deployment (BS placement

topology). In order to provide a comprehensive characterization of the SINR statistics, two extreme cases are studied. For one of the cases, the placement of BSs is optimized with a HEX deployment. Such cell deployment most likely may require extra engineering work to redesign the lighting infrastructure in a room, which may be more difficult to implement, but offers the best performance. For the other case, the placement of BSs is completely random. The 2-D spatial distribution of BSs follows a homogeneous PPP. The irregular placement of luminaries is mainly motivated by the following considerations: first, the placement of a luminary may be limited by the wiring structure in the room. Second, in some cases, non-uniform illumination is required, which means that the lighting is enhanced in certain parts of the room, but not in other parts. Also, even for a uniform cell deployment, some cells may not have users. In that case, the downlink transmission can be switched off, which results in a non-uniform active cell deployment. Due to practical issues, the cell deployments of these two extreme cases (HEX and PPP) would be very rare in practice. Therefore, similar to [37], we expect that the downlink SINR achieved by the system with PPP (HEX) cell deployment works as a lower (upper) bound for the cases with other potential cell deployments that may be used in practice. In different cell deployments, the shape of the cell varies. In order to guarantee a fair comparison, the average cell size of the systems with each cell deployment is scaled to be the same as a circular cell with a radius of R.

### A. System Model Simplification

In order to simplify the following analysis and to make the analysis tractable, the SINR expression (24) has to be modified. First, it is assumed that the non-linear characteristic of the relationship between the input current to the output optical power is minimized by using pre-distortion techniques [38], [39]. Therefore, a linear dynamic range from 0 to  $2I_{\rm DC}$  is considered. This leads to a clipping level of  $\lambda_{\rm t}=-\lambda_{\rm b}=\zeta$  and  $\mathbb{E}\left[U(x(t))\right]=0$ . In addition, the  $\mathbf{1}_{\textstyle \textstyle \prod_2}(x)$  function makes (24) a piecewise function, which causes extra mathematical complexity in the analysis. Therefore, the worst case with a full FOV of  $\psi_{\rm max}=90^\circ$  is assumed, thereby making  $\mathbf{1}_{\textstyle \textstyle \prod_2}(x)$  always equal to 1 in the region of interest. Then, the simplified SINR expression can be written as:

$$\gamma(k) = \left(\frac{\left(\rho^2 + \sigma_{\text{clip}}^2\right)\mathcal{I} + \mathcal{Z}(k)}{\rho^2 \mathcal{X}} + \frac{\sigma_{\text{clip}}^2}{\xi^2 \rho^2}\right)^{-1}, \quad (37)$$

where 
$$\mathcal{X}=\xi^2\left(r_0^2+h^2\right)^{-m-3}$$
 and  $\mathcal{I}=\sum\limits_{i\in\mathbf{M}}\left(r_i^2+h^2\right)^{-m-3}$ .

#### B. HEX Cell Deployment

Instead of considering a specified network in a room, an infinite extending HEX network is considered in this analysis. There are two reasons for considering this deployment. First, since the main concern in this study is CCI from neighboring BSs, the number of neighboring BSs causing CCI is maximized in an infinite network. Consequently, an infinite network should

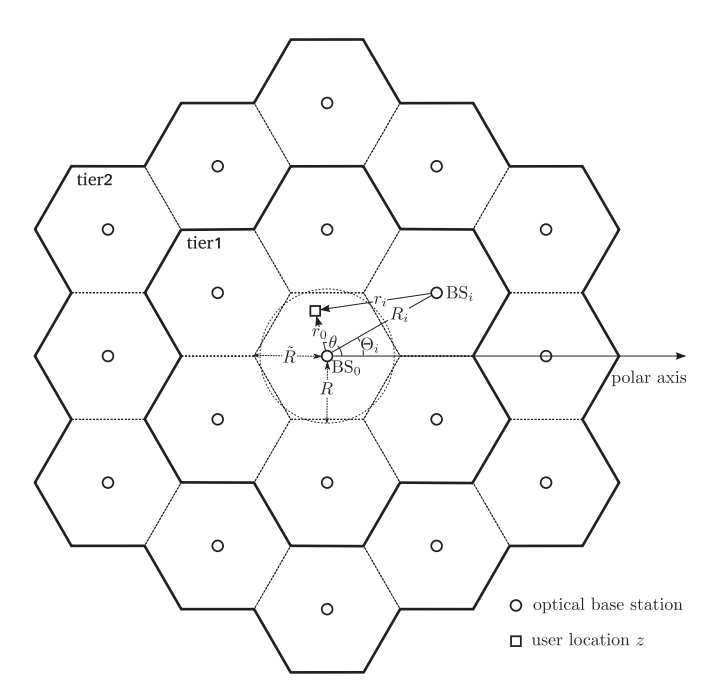


Fig. 9. Two-layer HEX network model with polar coordinates.

exhibit a worst case system performance. Second, removing the boundary effect of the network significantly reduces the complexity of the analysis. However, it is unnecessary to consider neighboring BSs that are too far away from the considered cell as they cause negligible CCI to the considered users and cause greater analysis complexity. Instead, a two-layer HEX cellular cell deployment is considered to approximate the infinite network as shown in Fig. 9 and the user performance in the central cell is analyzed. In this study, all networks are assumed to be heavily loaded. In addition, the cases with  $\Delta = 1$  and  $\Delta = 3$ are considered, since these cases are more likely to be used in practice. In this model, a polar coordinate system is used to represent the location of the user and BSs. Each 2-D location has a specified distance to the origin and a polar angle. A user at zis  $r_0$  away from the origin and has a polar angle of  $\theta$ , as shown in Fig. 9. Similarly, the ith BS is located at  $(R_i, \Theta_i)$ . In order to make the area of the HEX cell equal to that of the equivalent circular cell, the HEX cell radius satisfies  $\hat{R} \approx 1.1R$ , as shown in Fig. 9. Then the horizontal offset between the ith BS and the user at z can be calculated as:

$$r_i(z) = \sqrt{r_0^2 + R_i^2 - 2R_i r_0 \cos(\theta - \Theta_i)}.$$
 (38)

The user at  $z=(r_0,\theta)$  in the central cell is served by the 0th BS. The remaining BSs using the same transmission resource  $(i\in H)$  causes CCI to the desired user at z. Since the coordinates of all BSs are known, by inserting (38) into (37), the SINR  $\gamma(k)$  can be calculated as a function of the user location z. Thus, the statistics of the SINR can be converted from the random distribution of user location z. Since the users are uniformly distributed in the cell, the PDFs of  $r_0$  and  $\theta$  follow:  $f_{r_0}(r_0) = \frac{2r_0}{R^2}$  and  $f_{\theta}(\theta) = \frac{1}{2\pi}$ , respectively. The objective is defined as  $\mathbb{P}\left[\gamma(k) < T\right]$ , which calculates the probability that the downlink SINR is less than a threshold T. Using (37) and conditioning on

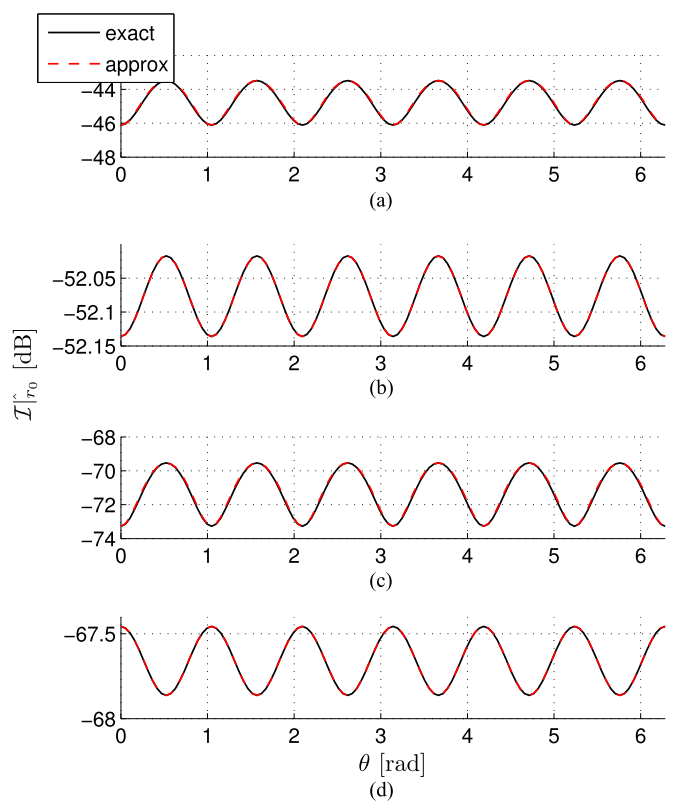


Fig. 10. CCI term approximation. In configuration (a) R=3 m,  $\Delta=1$  and r=R m. m is calculated using (36). Relative to configuration (a), configuration (b) changes r to R/2, configuration (c) changes R to 2 m, and configuration (d) changes  $\Delta$  to 3.

 $r_0$ , this yields:

$$\mathbb{P}[\gamma(k) < T | r_0] = \mathbb{P}\left[\mathcal{I} > \frac{\rho^2 \mathcal{X}\left(\frac{1}{T} - \frac{\sigma_{\text{elip}}^2}{\rho^2 \xi^2}\right) - \mathcal{Z}(k)}{\rho^2 + \sigma_{\text{elip}}^2} \middle| r_0\right]. \tag{39}$$

The combination of (38) and (37) makes  $\mathcal{I}$  an extremely complex function of  $\theta$  for carrying out a PDF transformation. Therefore, this relationship between  $\mathcal{I}$  and  $\theta$  should be simplified in order to make the calculation tractable. Fig. 10 shows the CCI term  $\mathcal{I}$  in a HEX network against  $\theta$  with a given  $r_0$ . It can be observed that with the increase of  $\theta$ ,  $\mathcal{I}(\theta|r_0)$  oscillates between two extreme values with a period of 60°. This is because of the central symmetric deployment of the interfering BSs. Therefore, an approach that is similar to the "flower" model introduced in [40] is used to simplify the relationship between  $\mathcal{I}$  and  $\theta$ . The concept is to use a cosine function to approximate the oscillation of the function  $\mathcal{I}(\theta|r_0)$ . First,  $\mathcal{I}_{0^{\circ}}(r_0)$  and  $\mathcal{I}_{30^{\circ}}(r_0)$  are calculated, which are the function  $\mathcal{I}$  of  $r_0$  assuming a  $\theta$  of  $0^{\circ}$ and of 30°, respectively. Both values constitute the oscillation bounds of the function  $\mathcal{I}(\theta|r_0)$ . The expressions for  $\mathcal{I}_{0^{\circ}}(r_0)$  and  $\mathcal{I}_{30^{\circ}}(r_0)$  can be calculated in a closed form, as shown in Appendix A. Then, the approximated CCI term can be calculated using the following expression:

$$\hat{\mathcal{I}} = \frac{\mathcal{I}_{30^{\circ}}(r_0) + \mathcal{I}_{0^{\circ}}(r_0)}{2} + \frac{|\mathcal{I}_{30^{\circ}}(r_0) - \mathcal{I}_{0^{\circ}}(r_0)|}{2} \cos(6\theta). \tag{40}$$

Fig. 10 compares the exact conditional CCI term  $\mathcal{I}(\theta|r_0)$  to the approximated one  $\hat{\mathcal{I}}(\theta|r_0)$  with different system configurations. In the system with each of the configurations, the approximated model  $\hat{\mathcal{I}}(\theta|r_0)$  matches well with the exact model  $\mathcal{I}(\theta|r_0)$ . The difference between the two curves is minimal as shown in each plot of Fig. 10. Thus, it is reasonable to replace  $\mathcal{I}$  with  $\hat{\mathcal{I}}$ . By replacing  $\mathcal{I}$  in (39) with (40), the conditional probability  $\mathbb{P}[\gamma(k) < T|r_0]$  can be written as:

$$\mathbb{P}[\gamma(k) < T|r_0] =$$

$$\mathbb{P}\left[\cos(6\theta) > \frac{2\rho^2 \mathcal{X}\left(\frac{1}{T} - \frac{\sigma_{\text{clip}}^2}{\rho^2 \xi^2}\right) - 2\mathcal{Z}(k)}{\left(\rho^2 + \sigma_{\text{clip}}^2\right) |\mathcal{I}_{30^\circ} - \mathcal{I}_{0^\circ}|} - \frac{\mathcal{I}_{30^\circ} + \mathcal{I}_{0^\circ}}{|\mathcal{I}_{30^\circ} - \mathcal{I}_{0^\circ}|} \middle| r_0\right]$$

$$= \frac{1}{2} - \frac{1}{\pi} \arcsin^{\dagger} \left( \frac{2\rho^{2} \mathcal{X} \left( \frac{1}{T} - \frac{\sigma_{\text{elip}}^{2}}{\rho^{2} \xi^{2}} \right) - 2\mathcal{Z}(k)}{\left( \rho^{2} + \sigma_{\text{elip}}^{2} \right) |\mathcal{I}_{30^{\circ}} - \mathcal{I}_{0^{\circ}}|} - \frac{\mathcal{I}_{30^{\circ}} + \mathcal{I}_{0^{\circ}}}{|\mathcal{I}_{30^{\circ}} - \mathcal{I}_{0^{\circ}}|} \right), \tag{41}$$

where

$$\arcsin^{\dagger}(x) = \begin{cases} 1 & : x > 1\\ \arcsin(x) : |x| \le 1 \\ -1 & : x < -1 \end{cases}$$
 (42)

The final CDF of SINR can be calculated by averaging (41) over  $r_0$  as described in (43), which can be solved efficiently by using numerical methods. In this integration, the range of  $r_0$  is from 0 to R, which corresponds to the integration over the equivalent circular cell. This approximation is made for simplicity.

$$\mathbb{P}[\gamma(k) < T] = \int_{0}^{R} f_{r_{0}}(r_{0}) \mathbb{P}[\gamma(k) < T | r_{0}] dr_{0}$$

$$= \int_{0}^{R} \frac{r_{0}}{R^{2}} - \frac{2r_{0}}{\pi R^{2}} \arcsin^{\dagger}$$

$$\times \left( \frac{2\rho^{2} \mathcal{X} \left( \frac{1}{T} - \frac{\sigma_{\text{clip}}^{2}}{\rho^{2} \xi^{2}} \right) - 2\mathcal{Z}(k)}{\left( \rho^{2} + \sigma_{\text{clip}}^{2} \right) |\mathcal{I}_{30^{\circ}} - \mathcal{I}_{0^{\circ}}|} \right)$$

$$- \frac{\mathcal{I}_{30^{\circ}} + \mathcal{I}_{0^{\circ}}}{|\mathcal{I}_{20^{\circ}} - \mathcal{I}_{0^{\circ}}|} dr_{0}. \tag{43}$$

## C. PPP Cell Deployment

Similar to the HEX network, an infinite extending network is considered. However, the origin of the coordinates is placed at a random user [37]. The horizontal positioning of the nearby optical BSs follows a 2-D homogeneous PPP with a density of  $\Lambda$ , as shown in Fig. 11. In the PPP case, a similar method is used to retrieve the SINR statistics by calculating  $\mathbb{P}[\gamma(k) < T|r_0]$  using (39). Similar to the case of HEX network, the distribution of  $\mathcal I$  is necessary. The exact distribution of  $\mathcal I$  is complicated to solve. However, the method presented in [41] can be used to calculate the characteristic function (CF) of  $\mathcal I$  conditioned on  $r_0$ . The details are as follows.

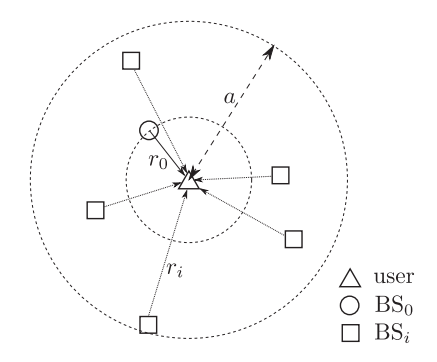


Fig. 11. PPP network geometry.

Since there is no dependency between BSs, the only significant variable in this model is the Euclidean distance between a BS and the user  $D_i$ . According to the geometry shown in Fig. 3, the CCI term  $\mathcal{I}$  in (37) can be rewritten as:  $\mathcal{I} = \sum g(D_i)$ , where  $g(x) = x^{-2(m+3)}$ . It is assumed that the furthest BS is a away from the user and the interfering BS is not closer than the desired BS which is  $r_0$  away from the user. As shown in Fig. 11,  $r_i$  is within the range of  $[r_0, a]$ . Since the interfering BSs are uniformly distributed, then the PDF of  $r_i$  can be found as:

$$f_{r_i}(r_i) = \frac{2r_i}{a^2 - r_0^2}, \ r_0 \le r_i \le a.$$
 (44)

Then the PDF of  $D_i$  can be calculated using the PDF transformation rule from (44) as:

$$f_{D_i}(D_i) = \frac{2D_i}{a^2 - r_0^2}, \ \sqrt{r_0^2 + h^2} \le D_i \le \sqrt{a^2 + h^2}.$$
 (45)

The conditional CF of  $\mathcal{I}$  is defined as  $\varphi_{\mathcal{I}_a}(\omega|r_0) = \mathbb{E}\left[\mathrm{e}^{j\omega\mathcal{I}_a}\right]$ . Since the number of interfering BSs I is a non-negative integer random variable,  $\varphi_{\mathcal{I}_a}(\omega)$  can be extended as:

$$\varphi_{\mathcal{I}_a}(\omega|r_0) = \mathbb{E}_I\left[\mathbb{E}\left[e^{j\omega\mathcal{I}_a}|I=n\right]\right].$$
(46)

Since each  $D_i$  in  $\mathcal{I}$  is independent of each other,  $\varphi_{\mathcal{I}_a}(\omega)$  conditioned on I can be factorized as follows:

$$\mathbb{E}\left[e^{j\omega\mathcal{I}_a}|I=n\right] = \prod_{i=1}^n \mathbb{E}\left[e^{j\omega g(D_i)}\right]$$
$$= \left(\int_{\sqrt{r_0^2 + h^2}}^{\sqrt{a^2 + h^2}} \frac{2De^{j\omega g(D)}}{a^2 - r_0^2} dD\right)^n. \quad (47)$$

Because I follows a Poisson distribution with a mean of  $\frac{\Lambda}{\Delta}$ , the corresponding probability mass function of I can be written as follows:

$$\mathbb{P}[I=n] = \frac{e^{-\frac{\Lambda\pi}{\Delta}\left(a^2 - r_0^2\right)} \left(\frac{\Lambda\pi}{\Delta}\left(a^2 - r_0^2\right)\right)^n}{n!}.$$
 (48)

Next, (46) can be extended as:

$$\varphi_{\mathcal{I}_{a}}(\omega|r_{0}) = \sum_{n=0}^{\infty} \mathbb{P}[I=n]\mathbb{E}\left[e^{j\omega\mathcal{I}_{a}}|I=n\right]$$

$$= e^{-\frac{\Lambda\pi}{\Delta}\left(a^{2}-r_{0}^{2}\right)}\sum_{n=0}^{\infty}\frac{1}{n!}$$

$$\left(\frac{\Lambda\pi}{\Delta}\int_{\sqrt{r_{0}^{2}+h^{2}}}^{\sqrt{a^{2}+h^{2}}}2De^{j\omega g(D)}dD\right)^{n}$$

$$\stackrel{(a)}{=} e^{-\frac{\Lambda\pi}{\Delta}\left(a^{2}-r_{0}^{2}-\int_{\sqrt{r_{0}^{2}+h^{2}}}^{\sqrt{a^{2}+h^{2}}}2De^{j\omega g(D)}dD\right)}, \quad (49)$$

where (a) uses the Taylor series for  $e^x$ . By limiting  $a \to \infty$ , the CF can be calculated as follows:

$$\varphi_{\mathcal{I}}(\omega|r_0) = \exp\left(\sum_{n=1}^{\infty} \frac{(j\omega)^n}{n!} \frac{\Lambda \pi \left(r_0^2 + h^2\right)^{1 - n(m+3)}}{\Delta(n(m+3) - 1)}\right). (50)$$

The proof for (50) is provided in Appendix IX-B. Theoretically, (50) can be converted to the corresponding PDF. However, this operation is intractable. Therefore, an alternative approximation approach is used to obtain the PDF of CCI. Since the cumulant generating function can be written as:

$$\ln\left(\varphi_{\mathcal{I}}(\omega)\right) = \sum_{n=1}^{\infty} \kappa_n(\mathcal{I}) \frac{(j\omega)^n}{n!}.$$
 (51)

By comparing (51) and (50), the nth cumulant of  $\mathcal{I}$  conditioning on  $r_0$  can be found as:

$$\kappa_n^{\mathcal{I}} = \frac{\Lambda \pi \left(r_0^2 + h^2\right)^{1 - n(m+3)}}{\Delta (n(m+3) - 1)}.$$
 (52)

With all cumulants known, the corresponding nth raw moment can be calculated recursively by the following set of equations:

$$\mu_n = \begin{cases} 1 & : n = 0 \\ \kappa_1 & : n = 1 \\ \kappa_n + \sum_{l=1}^{n-1} {n-1 \choose l-1} \kappa_l \mu_{n-l} : n \ge 2 \end{cases}$$
 (53)

With all moments of the CCI distribution known, an expansion of the PDF as a sum of Gamma densities proposed in [42] can be used. This expansion is based on the Gram-Charlier series and Laguerre polynomials. The Gamma density used in this expansion is  $f_V(v) = \frac{v^{\alpha-1} \mathrm{e}^{-v}}{\Gamma(\alpha)}$  for a random variable V. The expansion of the PDF is given as [42]:

$$f_V(v) = \frac{v^{\alpha - 1} e^v}{\Gamma(\alpha)} \sum_{n=0}^{\infty} \mathcal{A}_n \mathcal{L}_n^{\alpha}(v),$$
 (54)

where the Laguerre polynomial  $\mathcal{L}_n^{\alpha}(v)$  can be calculated as:

$$\mathcal{L}_n^{\alpha}(v) = (-1)^n v^{1-\alpha} e^v \frac{\mathrm{d}^n}{\mathrm{d}v^n} \left( v^{n+\alpha-1} e^{-v} \right)$$
$$= \sum_{l=0}^n \binom{n}{l} (-1)^{n-l} v^l S_l^n, \tag{55}$$

where l is a non-negative integer, and

$$S_l^n = \begin{cases} 1 & : l > n-1 \\ \prod_{\iota=l}^{n-1} (\alpha + \iota) : l \le n-1 \end{cases}$$
 (56)

The coefficients  $A_n$  in (54) can be calculated using the following expression:

$$\mathcal{A}_{n} = \frac{\Gamma(\alpha)}{n!\Gamma(\alpha+n)} \int_{0}^{\infty} f_{V}(v) \mathcal{L}_{n}^{\alpha}(v) dv$$

$$= \frac{(-1)^{n}\Gamma(\alpha)}{n!\Gamma(\alpha+n)} \sum_{l=0}^{n} {n \choose l} (-1)^{l} S_{l}^{n} \int_{0}^{\infty} v^{l} f_{V}(v) dv$$

$$= \frac{(-1)^{n}\Gamma(\alpha)}{n!\Gamma(\alpha+n)} \sum_{l=0}^{n} {n \choose l} (-1)^{l} S_{l}^{n} \mu_{l}^{V}.$$
(57)

The expansion (54) requires the random variable V to have its mean and variance equal to  $\alpha$ :

$$\mathbb{E}[V] = \sigma_V^2 = \alpha. \tag{58}$$

Therefore, the CCI random variable  $\mathcal{I}$  has to be scaled to satisfy the condition in (58). So  $V = \beta \mathcal{I}$  is defined, where  $\beta$  is the scaling factor. Then the cumulants and moments of V should follow:

$$\kappa_n^V = \beta^n \kappa_n^{\mathcal{I}},\tag{59}$$

$$\mu_n^V = \beta^n \mu_n^{\mathcal{I}}. \tag{60}$$

Note that  $\kappa_1^{\mathcal{I}}$  and  $\kappa_2^{\mathcal{I}}$  are equal to the mean and variance of  $\mathcal{I}$ , respectively. Then the mean and variance of V should be  $\beta \kappa_1^{\mathcal{I}}$  and  $\beta^2 \kappa_2^{\mathcal{I}}$ , respectively. The value of  $\alpha$  and  $\beta$  can be calculated in conjunction with (52) and (58) as:

$$\beta = \frac{(2m+5)\left(r_0^2 + h^2\right)^{m+3}}{m+2},\tag{61}$$

$$\alpha = \beta \kappa_1^{\mathcal{I}} = \beta^2 \kappa_2^{\mathcal{I}} = \frac{\Lambda \pi (2m+5) (r_0^2 + h^2)}{\Delta (m+2)^2}.$$
 (62)

By substituting  $\beta \mathcal{I}$  for V in (54) and after rearranging, the conditional PDF  $f_{\mathcal{I}}(\mathcal{I}|r_0)$  can be determined as follows:

$$f_{\mathcal{I}}(\mathcal{I}|r_0) = \sum_{n=0}^{\infty} \left( \sum_{l_1=0}^n \frac{\beta^{\alpha} C_{l_1}^n \mu_{l_1}^{\mathcal{I}}}{n! \Gamma(\alpha+n)} \right) \left( \sum_{l_2=0}^n \frac{C_{l_2}^n \mathcal{I}^{l_2+\alpha-1}}{e^{\beta \mathcal{I}}} \right), \tag{63}$$

where

$$C_l^n = \binom{n}{l} (-1)^{n-l} \beta^l S_l^n. \tag{64}$$

Next, the probability

$$\mathbb{P}\left[\mathcal{I} > \tilde{\mathcal{I}}|r_{0}\right] = \int_{\tilde{\mathcal{I}}}^{\infty} f_{\mathcal{I}}(\mathcal{I}|r_{0}) d\mathcal{I}$$

$$= \sum_{n=0}^{\infty} \left(\sum_{l_{1}=0}^{n} \frac{\beta^{\alpha} C_{l_{1}}^{n} \mu_{l_{1}}^{\mathcal{I}}}{n!\Gamma(\alpha+n)}\right)$$

$$\times \left(\sum_{l_{2}=0}^{n} \frac{C_{l_{2}}^{n}}{\beta^{l_{2}+\alpha}} \Gamma\left(l_{2}+\alpha, \beta\tilde{\mathcal{I}}\right)\right), \quad (65)$$

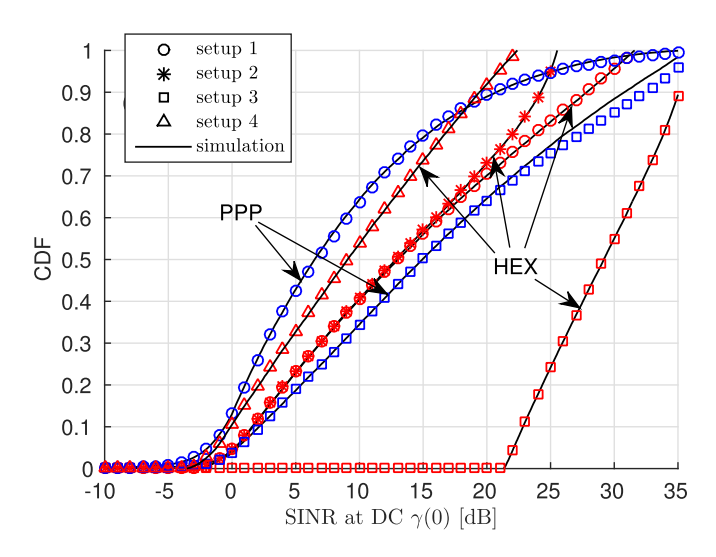


Fig. 12. The CDF of the SINR at DC. Setup 1: R=2.5~m,  $\phi_{1/2}=40^\circ$ ,  $\Delta=1,100\%$  output. Setup 2: same as setup 1 except  $\zeta=2.5$ . Setup 3: R=3~m,  $\phi_{1/2}=50^\circ$ ,  $\Delta=3,100\%$  output. Setup 4: same as setup 1 except 15% output and 1000~lux ambient light illuminance. Other parameters are listed in Table I if they are not specified.

where  $\Gamma(\nu,\epsilon)=\int_{\epsilon}^{\infty}\mathrm{e}^{-x}x^{\nu-1}\mathrm{d}x$  is the upper incomplete Gamma function; and

$$\tilde{\mathcal{I}} = \frac{\rho^2 \mathcal{X} \left( \frac{1}{T} - \frac{\sigma_{\text{clip}}^2}{\rho^2 \xi^2} \right) - \mathcal{Z}(k)}{\rho^2 + \sigma_{\text{clip}}^2}.$$
 (66)

Because  $r_0$  equals the distance between the user (origin) and the serving BS (closest node to origin), the PDF of  $r_0$  with node density of  $\Lambda$  should be  $f_{r_0}(r_0,\Lambda)=2\pi\Lambda r_0\mathrm{e}^{-\Lambda\pi r_0^2}$  in a PPP [43]. The final SINR CDF can be calculated by combining (65) with (39) and averaging  $\mathbb{P}[\gamma(k) < T|r_0]$  over  $r_0$  as (67).

$$\mathbb{P}[\gamma(k) < T] = \int_0^\infty f_{r_0}(r_0, \Lambda) \mathbb{P}[\gamma(k) < T | r_0] dr_0$$

$$= \int_0^\infty \frac{2\pi \Lambda r_0}{e^{\pi \Lambda r_0^2}} \sum_{n=0}^\infty \left( \sum_{l_1=0}^n \frac{\beta^\alpha C_{l_1}^n \mu_{l_1}^T}{n! \Gamma(\alpha + n)} \right)$$

$$\times \left( \sum_{l_2=0}^n \frac{C_{l_2}^n \Gamma\left(l_2 + \alpha, \beta \tilde{\mathcal{I}}\right)}{\beta^{l_2 + \alpha}} \right) dr_0. \tag{67}$$

Note that there is a summation with infinite upper bound in (67) which makes the calculation intractable. Therefore, the infinity upper bound of the summation is replaced by a finite integer number N. With the increase of N, (67) quickly converges to the case of  $N=\infty$ . When calculating the results, N=10 is found to be sufficient to provide accurate analytical results. With this approach, (67) can be solved using numerical methods.

#### D. SINR Statistics Results and Discussions

Fig. 12 shows the CDF of the SINRs at dc achieved by different system setups considering HEX and PPP cell deployments. The SINR at DC is shown as an example. The SINR at other frequencies decreases with an increase of frequency due to the low-pass effect of the front-end devices. The values shown in

TABLE I

Parameters	Symbol	Values	
Vertical Separation	h	2.25 [m]	
Receiver FOV	$\psi_{\mathrm{max}}$	90°	
Sampling frequency	$F_{ m s}$	360 [MHz]	
Front-end device bandwidth factor	$F_{\mathrm{fe}}$	31.7 [MHz]	
DC-bias level	ζ	3.2	
PD responsivity	$\eta_{ m pd}$	0.4 [A/W]	
PD physical area	$A_{\rm pd}$	$1  [{ m cm}^{ 2}  ]$	
Number of subcarriers	$\dot{K}$	512	
Power decrease factor	$\sigma_{ m P}$	20 [dB]	
Cell center illuminance from BS	$E_{\rm v}$	500 [lux]	
illuminance from ambient light	$E_{\rm v,ab}$	100 [lux]	
Absolute temperature	T	300 [K]	
Receiver load resistance	$R_{\rm L}$	500 [Ω]	

Table I are used if the system parameter is not specified for each setup, where the configuration of  $F_{\rm s}$  and  $F_{\rm fe}$  are in accordance with the setup in [13]. The configuration of  $\sigma_{\rm P}$  is justified in Section III-C. It can be found that the numerical results calculated using (43) and (67) agree with the corresponding Monte Carlo simulation in the region of interests.

In setup 1, R=2.5 m,  $\phi_{1/2}=40^{\circ}$  and  $\Delta=1$ . The results for both the HEX and the PPP networks are shown. It can be observed that with the same system configuration, a PPP network performs worse than a HEX network. In addition, the considered ambient light level is 100 lux in illuminance. Therefore, the BSs works with their full power to provide enough illumination. The highest SINR of above 30 dB shows that the noise at the receiver side causes little effect to the system performance. In setup 2, the DC-bias level is modified to 2.5. This results in a higher signal clipping level. Consequently, the highest SINR in this system is limited by the clipping noise. In setup 3, R=3 m,  $\phi_{1/2}=50^{\circ}$ ,  $\Delta=3$ . Other parameters are the same as setup 1. The high reuse factor leads to a lower level of CCI and the overall SINR level improved significantly compared with that of setup 1. Therefore, the corresponding SINR is improved compared to the case of setup 1 for both HEX and PPP networks. Setup 4 considers a special case with sufficient illumination from ambient light with a illuminance of 1000 lux. Thus, the BS works in a dimmed mode with only 15% of its normal output. Due to the reduced signal power and increased noise level, the overall SNR level is decreased ( $-3 \, dB - 22 \, dB$ ). This demonstrates that the system will work in strong ambient light conditions, and even in dimmed mode. Furthermore, energy-efficient modulation techniques such as eU-OFDM [12] may be used to further improve performance when the lights are dimmed.

#### V. CELL DATA RATE AND OUTAGE PROBABILITY

In this section, the average cell data rate and outage probability are calculated and analyzed. Since the information about the per subcarrier SINR and its statistics is known, different modulation and coding schemes can be assigned to each subcarrier adaptively according to the value of  $\gamma(k)$ . The average

TABLE II				
ADAPTIVE MODULATION AND CODING				

	AMC1		AMC2	
n	$T_n$ [dB]	$\varepsilon_n$ [bits/symbol]	$T_n$ [dB]	$\varepsilon_n$ [bits/symbol]
0	_	0	_	0
1	9.8	2	-6	0.1523
2	13.4	3	-5	0.2344
3	16.5	4	-3	0.3770
4	19.6	5	-1	0.6016
5	22.5	6	1	0.8770
6	25.5	7	3	1.1758
7	28.4	8	5	1.4766
8	-	_	8	1.9141
9	-	_	9	2.4063
10	-	_	11	2.7305
11	_	_	12	3.3223
12	_	_	14	3.9023
13	-	_	16	4.5234
14	_	_	18	5.1151
15	-	-	20	5.5547

achievable data rate in an optical attocell can be calculated using:

$$s = \frac{1}{\Delta} \sum_{k=1}^{K/2-1} \sum_{n=1}^{N} W_{\mathrm{sc}} \varepsilon_n \mathbb{P}[T_n < \gamma(k) < T_{n+1}]$$

$$= \frac{F_{s}}{\Delta K} \sum_{k=1}^{\frac{K}{2}-1} \sum_{n=1}^{N} \varepsilon_{n} \left( \mathbb{P}[\gamma(k) < T_{n+1}] - \mathbb{P}[\gamma(k) < T_{n}] \right), \quad (68)$$

where  $W_{\rm sc}$  is the bandwidth on each subcarrier;  $\varepsilon_n$  is the spectral efficiency (bits/symbol) of the  $n{
m th}$  adaptive modulation and coding (AMC) level; and  $T_n$  is the corresponding minimum required SINR to achieve  $\varepsilon_n$ . In this study, two AMC schemes are considered, which are listed in Table II. The AMC scheme 1 is the uncoded QAM modulation [44] achieving a maximum bit error rate target of  $1\times 10^{-3}$ . This scheme is reliable and simple to implement, and has been used in several experimental studies [9], [13], [14]. However, this scheme achieves a relatively low spectral efficiency and the minimum required SINR is as high as 9.8 dB. The AMC scheme 2 is used in the long term evolution (LTE) system [45], which is more spectrally efficient, and the lowest acceptable SINR is -6 dB. However, it is more complex to implement.

Outage probability is defined as the probability that the received signal SINRs on all subcarriers are below the lowest SINR requirement for an AMC scheme. Since we know that the value of  $\gamma(1)$  is the highest among the SINR on the all the subcarriers, the outage probability can be calculated as:

$$\mathcal{P}_{\text{out}} = \mathbb{P}[\gamma(1) < T_1]. \tag{69}$$

Next, the accuracy of the cell data rate calculation is evaluated and the cell data rate/outage probability performance of an optical attocell is analyzed. The results include the systems with the HEX/PPP network model and the system with reuse factor of  $\Delta=1$  and  $\Delta=3.$  The cell radius R and the sampling frequency (modulation bandwidth)  $F_{\rm s}$  are considered as the variables for study. Fig. 13 shows the cell data rate against

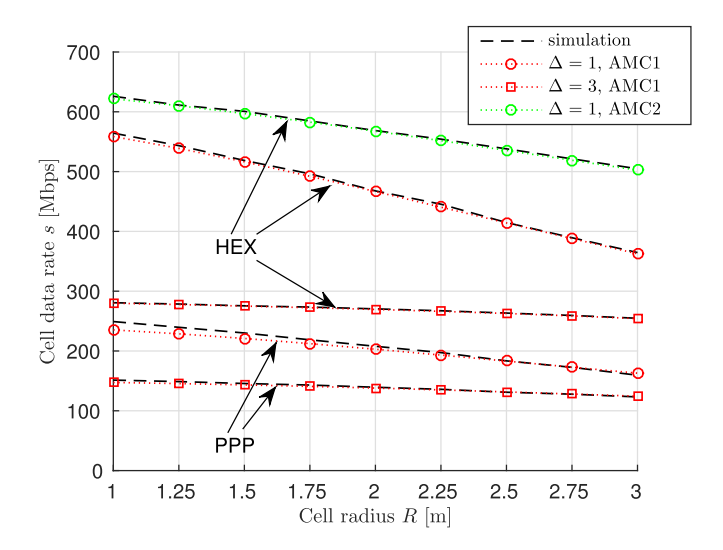


Fig. 13. Achievable cell data rate against cell radius R. The emission order m is configured based on (36). Other system parameters are listed in Table I if not specified.

the cell radius R. As shown in Section IV-D, a network operating with full BS power will not be limited by noise. Therefore, according to the analysis in Section III-C, the emission order m is configured based on (36) to achieve a better performance. Other system parameters are the same as those listed in Table I if they are not specified. For all of the systems, the Monte Carlo simulation results show close agreement with the analytical calculations, which prove the accuracy of (68). As expected, a HEX network system performs better than a PPP network system with the same remaining system configuration. The cell data rate generally decreases with the increase of R. This is because a system with a smaller cell has a higher value of m according to (36), which introduces less CCI to nearby BSs. First, the system using AMC1 is considered. With the same cell deployment, the system with  $\Delta = 1$  always achieves a higher data rate than the system with  $\Delta = 3$ . In the case of the HEX cell deployment, the  $\Delta = 1$  system achieves 40% to 100% higher data rate than the  $\Delta = 3$  system. However, the  $\Delta = 1$  system always has a much higher outage probability than the  $\Delta = 3$  system as shown in Fig. 14. For example, in the case of the HEX cell deployment, the  $\Delta = 1$  system has an outage probability of about 30% - 45%. In contrast, the  $\Delta = 3$  system has an outage probability of zero. In Section IV, it has been demonstrated that a  $\Delta = 1$  system with an appropriate configuration, the minimum SINR can be kept above -5 dB. Therefore, using AMC2 in a HEX network, the zero outage probability can be achieved even with  $\Delta = 1$ . In addition, the cell data rate is further improved by 60 Mb/s to 140 Mb/s.

The relationship between cell data rate/outage probability and the sampling frequency (modulation bandwidth) is examined, as shown in Figs. 15 and 16. A cell radius of R=2.5 m, a half-power semi-angle of  $\phi_{1/2}=40^\circ$  and AMC1 are used in this system. Other system parameters are the same as those listed in Table I if they are not specified. With an increase of the sampling frequency  $F_{\rm s}$ , the cell data rate increases when sampling frequency is low. This is because the more bandwidth

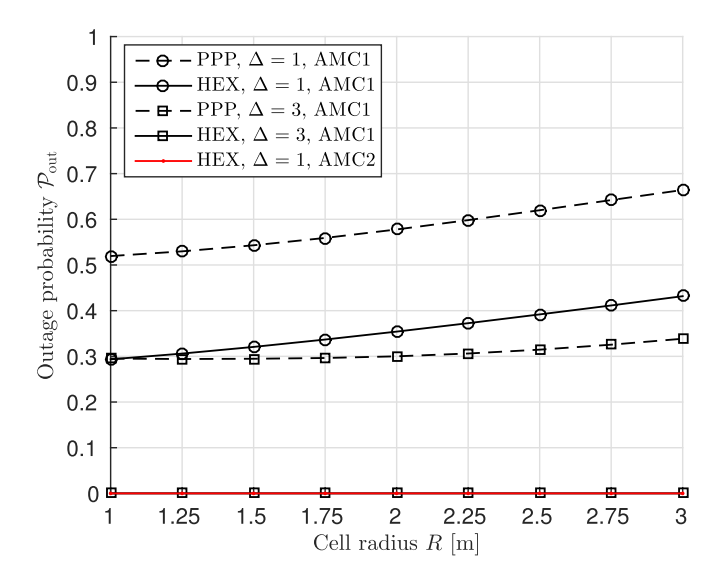


Fig. 14. Outage probability against cell radius R. The emission order m is configured based on (36). Other system parameters are listed in Table I if not specified.

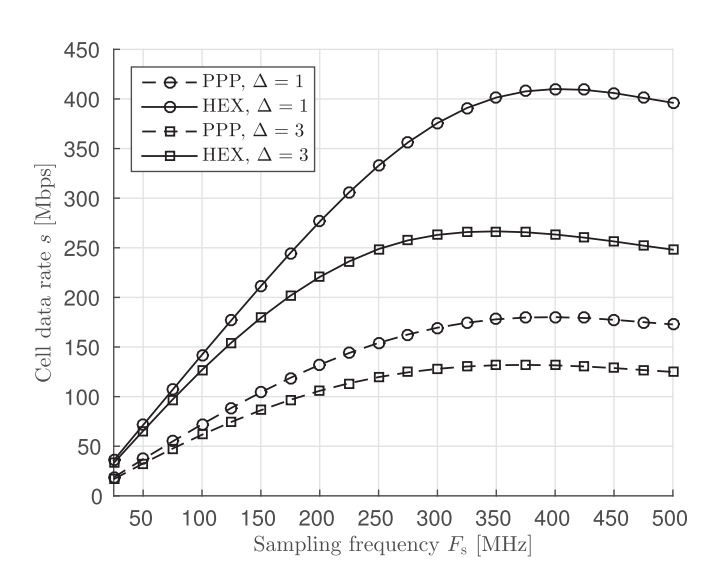


Fig. 15. Achievable cell data rate against sampling frequency  $F_{\rm s}$  with  $R=2.5~{\rm m},\,\phi_{1/2}=40^{\circ}$  and AMC1. Other parameters are listed in Table I if they are not specified.

that the system uses, the higher the data rate that the system can achieve. However, when the sampling frequency increases further, the channel quality on the high frequency subcarriers becomes worse. Meanwhile, the total transmission power is spread to a wider frequency band. Thus the signal power on each subcarrier decreases. Consequently, the increasing speed of the cell data rate with sampling frequency becomes slower. In addition, with a further increase of sampling frequency, the SINR of the cell edge user becomes below the threshold for transmission. Consequently, the outage probability also increases with the bandwidth increase, as shown in Fig. 16. When the sampling frequency is far beyond the 3-dB bandwidth, too much signal power is wasted on the subcarriers that are subject to unfavorable channel conditions with the degradation of the signal quality on

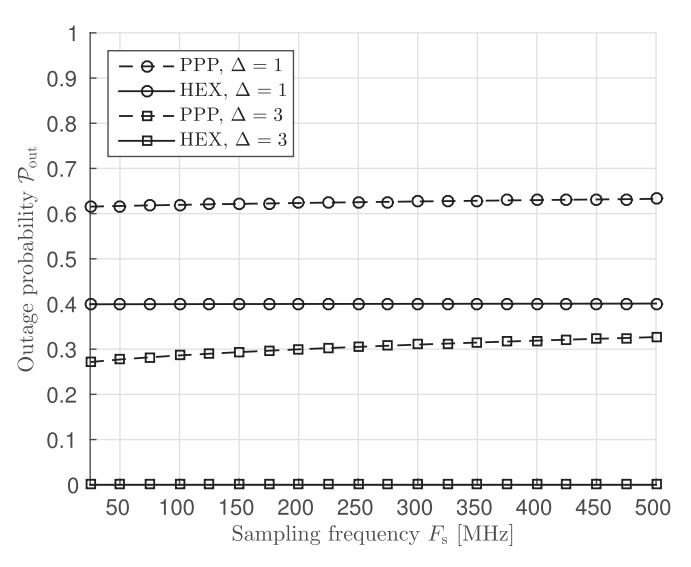


Fig. 16. Outage probability against sampling frequency  $F_{\rm s}$  with R=2.5 m,  $\phi_{1/2}=40^\circ$  and AMC1. Other parameters are listed in Table I if they are not specified.

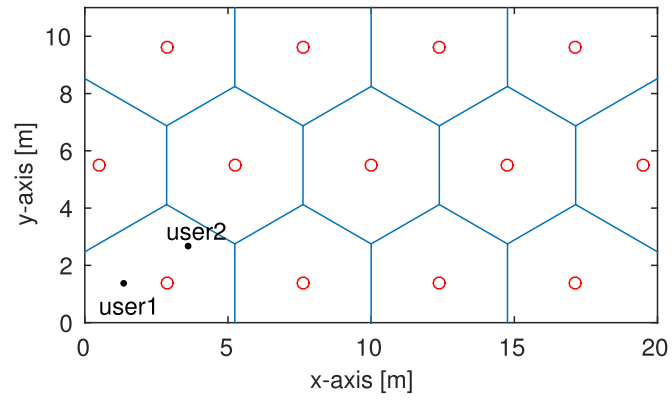


Fig. 17. Cell deployment of the finite HEX network in a room of size  $20~\rm m \times 11~m \times 3~m.$ 

the subcarriers which exhibit good channel conditions. Consequently, the cell data rate starts to decrease.

## VI. PERFORMANCE OF FINITE NETWORKS AND MP EFFECT

In previous sections, infinite networks are analyzed to approximate the performance of the practical system. In this section, the performance of a finite network deployed in a room is compared with the corresponding infinite network with the same system configurations. The MP effects due to room internal surface reflections are considered here.

The considered finite network is deployed in a room of size  $20~\mathrm{m} \times 11~\mathrm{m} \times 3~\mathrm{m}$  with HEX model as shown in Fig. 17. The reflectivity of the ceiling and walls is 0.7, and the reflectivity of the floor is 0.3. A cell radius of  $R=2.5~\mathrm{m}$ , a half-power semi-angle of  $\phi_{1/2}=40^\circ$  and AMC2 are used in this system. The remaining parameters are as given in Table I if they are not specified. First, two typical users in a room edge cell in this finite HEX network are considered, as shown in Fig. 17. Both of the two users are  $1.5~\mathrm{m}$  away from the cell center and they are close to one of the edges of the hexagon cell boundary. A

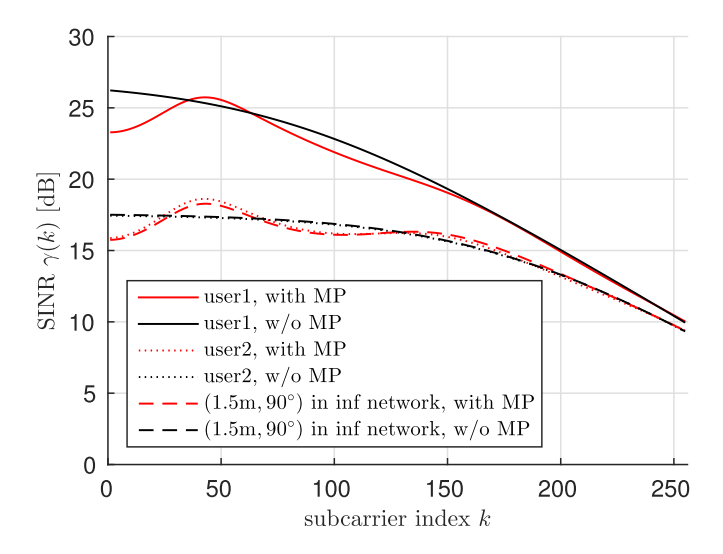


Fig. 18. SINR on subcarrier k. User 1 and user 2 are located at the bottom left cell in the considered finite network as shown in Fig. 17.

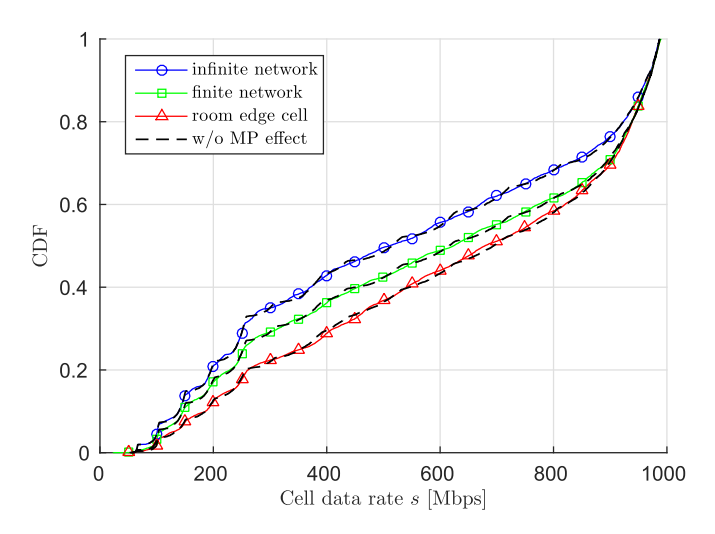


Fig. 19. Cell data rate statistics. AMC2 is used in these systems. The considered finite network corresponds to the system shown in Fig 17. The considered room edge cell corresponds to the cell in the bottom left cell shown in Fig 17.

third user at  $(1.5, 40^{\circ})$  in an infinity HEX network, denoted as user 3, corresponding to the positions of user 1 and user 2 is also considered for comparison. Fig. 18 shows the achieved SINR on each subcarrier with and without the MP effect. Due to the low-pass effect of the front-end device filtering, the achieved SINR decreases with the increase of subcarrier index. It can be observed that the SINRs calculated without MP effect offers a very close estimation to those calculated with MP effect for each user. Compared with user 2, user 1 is closer to the room edge and further away from the interfering BSs. Consequently, the overall SINR achieved by user 1 is much higher than that achieved by user 2. However, due to the stronger MP effect, the SINR calculated without MP effect slightly over-estimates the one with MP effect. In contrast, user 2 is closer to the room center, which is similar to the case in an infinite network. Therefore, the performances of user 2 and user 3 are very similar.

Next, the performance of this finite network in terms of data rate is considered. Fig. 19 shows the simulated statistics of the

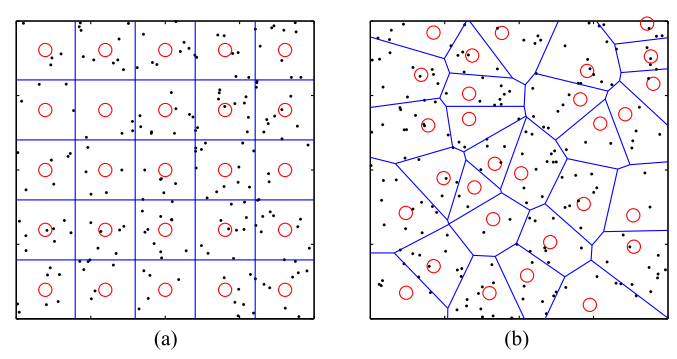


Fig. 20. Cell deployment for comparison. (a) Square network. (b) HCPP network.

cell data rate. Both the results with and without MP effect are simulated, and as shown, the MP effect does not cause any significant variance in the cell data rate performance of the systems. It can be observed that the infinite network offers the worst cell data rate. In contrast, the finite network achieves a slightly improved cell data rate. Furthermore, the cell data rate achieved in the room edge cell offers the highest cell data rate because of the lower CCI level. Therefore, it can be concluded that MP effect does not limit the performance of an optical attocell system. In addition, a worst case performance can be obtained by evaluating an infinite network.

## VII. SYSTEM PERFORMANCE COMPARISON WITH DIFFERENT CELL DEPLOYMENT

On the one hand, in a practical network arrangement where the existing lighting infrastructure is used, a BS layout with regular HEX lattice is possible but unlikely. On the other hand, a PPP network is also not entirely practical, because having light fixtures deployed in a completely random manner is not standard. In order to demonstrate the significance of the analyzed HEX/PPP network, the following two cell deployments are considered in addition in order to model typical optical attocell systems with potential cell deployments in practice.

#### A. Square Network

The first potential practical network model considered is the square lattice cellular model, in which BSs are placed on a square lattice, as shown in Fig. 20(a). This arrangement is common in indoor lighting network deployment for several reasons including design simplicity, good illumination uniformity and compliance with rectangular-shaped rooms. In the square network, the cell size is controlled by a parameter  $R_{\rm sq}$  which is defined as the distance between the two closest BSs. In order to have a fair comparison,  $R_{\rm sq}$  needs to be consistent with the circular cell radius R. This requires:  $R_{\rm sq} = \sqrt{A_{\rm cell}} = \sqrt{\pi R^2} \approx 1.77R$ .

## B. Hard-Core Point Process (HCPP) Network

In a PPP network, two BSs can be extremely close to each other, which is unlikely in practice. This is the main drawback of the PPP network model. Therefore, the Matérn type I HCPP is considered to approximate the network model, as shown in

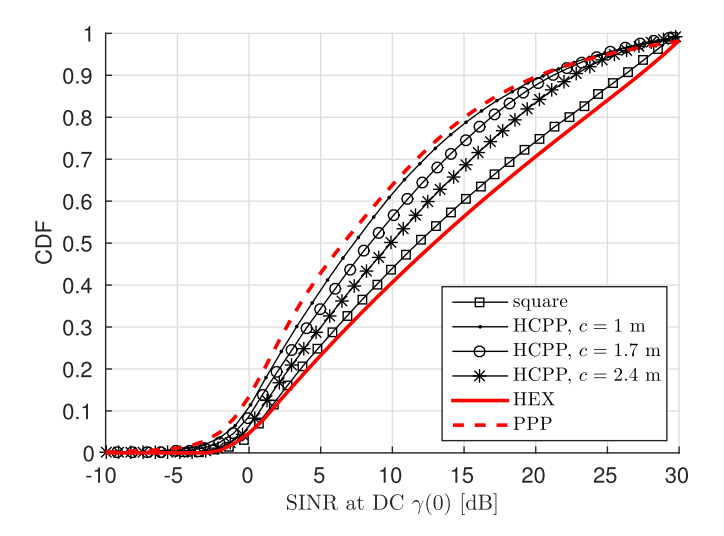


Fig. 21. Compare the SINR statistics at dc of systems with different cell deployments. An equivalent circular cell radius of R=3 m and a half-power semi-angle of  $\phi_{1/2}=40^\circ$  are used. For the results of the HCPP networks, c=1,1.7,2.4 m. Other parameters are listed in Table I.

Fig. 20(b). The HCPP is based on a PPP with the condition that the shortest distance between any two nodes is greater than a specified threshold, c. To generate a set of nodes according to a HCPP, a PPP with a density of  $\Lambda_0$  is applied. Then each point is tagged with a random number, and a dependent thinning process is carried out for each marked node as follows: retain the marked node if there is no other node within the circle centered at the marked node with a radius of c. After the thinning, the HCPP nodes density would be reduced. Therefore, to generate a HCPP with density of  $\Lambda$ , the initial PPP density  $\Lambda_0$  has to be [46]:  $\Lambda_0 = -\ln(1-\Lambda\pi c^2)/\pi c^2$ . In order to have a fair comparison, the configuration of  $\Lambda_0$  also has to make sure that the average cell area is the same as the equivalent circular cell area with the radius of R. Therefore,  $\Lambda_0 = -\ln(1-c^2/R^2)/\pi c^2$ .

## C. Performance Comparison

In Fig. 21, the CDF of the SINR at DC level of the systems with difference cell deployments are given and compared. An equivalent circular cell radius of R=3 m and a half-power semi-angle of  $\phi_{1/2}=40^\circ$  are used. The remaining system parameters are listed in Table I. Fig. 21 shows that the SINR distributions of the square network and HCPP network are bounded by the curves for the cases of the PPP network and the HEX network within the SINR region of interest. Similar to the conclusion drawn in [37], the SINR performance of a PPP (HEX) network can be considered as a lower (upper) bound for the case of practical optical attocell systems.

## VIII. OPTICAL ATTOCELL NETWORK VERSUS OTHER SMALL-CELL NETWORK

In this section, the performance of the optical attocell networks are compared to those achieved by RF femtocell networks and mmWave indoor networks. An optical attocell network achieves a high communication performance due to its extremely dense spatial reuse ( $R_{\rm atto} \in [1,3]$  m). Compared with

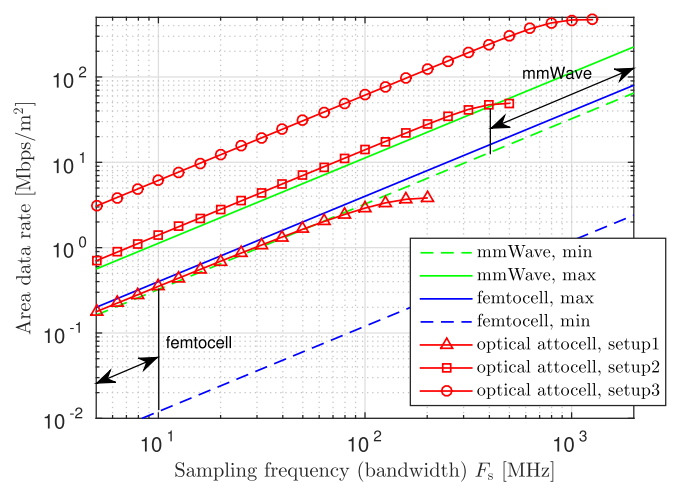


Fig. 22. Area data rate comparison among optical attocell networks, RF femtocell networks and mmWave networks. Optical attocell network setup 1: FE1 with  $F_{\rm fe}=15.2$  MHz, PPP network,  $\Delta=3$ , AMC1, R=2.5 m and  $\phi_{1/2}=40^\circ.$  Setup 2: FE3 with  $F_{\rm fe}=31.7$  MHz, HEX network,  $\Delta=1$ , AMC2, R=2 m and  $\phi_{1/2}=30^\circ.$  Setup 3: FE4 with  $F_{\rm fe}=81.5$  MHz, HEX network,  $\Delta=1$ , AMC2, R=1 m and  $\phi_{1/2}=15^\circ.$ 

RF femtocell systems, optical attocell networks have a relatively large license-free modulation bandwidth ( $100 \, \text{MHz}$  to  $> 1 \, \text{GHz}$ ) availability. In contrast, a femtocell has a relatively larger cell size  $(R_{\text{femto}} \in [10, 40] \text{ m})$  and a limited downlink bandwidth of about 10 MHz [3]. The modulation bandwidth of an indoor mmWave system, such as 60 GHz wireless personal area network, is generally in the range of 500 MHz to > 2 GHz, which is typically wider than that used by optical attocell networks. Therefore, a data rate of up to 7 Gb/s can be achieved by a mmWave system for a single link [47], while the maximum data rate that can be achieved by a single LED source is about 3 Gb/s [9]. However, due to hardware limitation and CCI issues, typically only one mmWave access point is available for each room. In contrast, multiple optical BSs can be installed in a room. This makes an optical attocell network advantageous in terms of data density. The benefits of high data density are obvious when a large number of devices in a room need high speed wireless service. To demonstrate the high data density achieved by an optical attocell system, a metric termed area data rate is defined as follows:

$$s_{\text{area}} = \frac{s}{A_{\text{cell}}}. (70)$$

Fig. 22 shows the area data rate performance of different systems. The results of the femtocell are extrapolated from [3], [5], [48], [49]. As shown, the indoor ASE achieved by the femtocell network is generally in the range from 0.03 to 0.0012 b/ (s·Hz·m²). With a bandwidth of 10 MHz, the area data rate achieved by femtocell networks is in the range from 0.012 to 0.3 Mb/(s·m²). The results of the mmWave systems are extrapolated from [47], [50], [51]. The spectral efficiency achieved by the mmWave system is generally in the range from 3.24 to 11.25 b/(s·Hz). Considering a room of size 10 m  $\times$  10 m, with a bandwidth in the range of 400 MHz to 2 GHz, the achievable area data rate is in the range of 13 to 225 Mb/(s·m²). The

estimated minimum and maximum values for these two systems are used as the benchmarks.

First, a low performance optical attocell system with setup 1 is considered, which uses the FE1 with  $F_{\rm fe}=15.2$  MHz and a PPP cell deployment with R=2.5 m,  $\phi_{1/2}=40^{\circ}$  and  $\Delta=3$ . The modulation and coding scheme is AMC1. Fig. 22 shows that the performance of this system is within the femtocell performance range. Note that the maximum achievable area data rate of  $3.82 \text{ Mb/(s} \cdot \text{m}^2)$  with a bandwidth of 200 MHz is much higher than those achieved by the femtocells with a bandwidth of 10 MHz. Note that the performance of the systems using different bandwidth is compared. This is because of the difference in the costs and availability of the two type of frequency bands. For the VLC system, the frequency band is totally unlicensed and does not cause any interference to a system in an adjacent frequency band. Therefore, there is no requirement for spectrum masks or leakages into neighboring bands used by other systems. In contrast, the RF resources are scarce and hence require tight spectrum masks. Next, two optical attocell systems with moderate (setup 2) and high (setup 3) performance are demonstrated. In setup 2, a HEX cell deployment with R=2 m,  $\phi_{1/2}=30^{\circ}$ ,  $\Delta = 1$  and AMC2 is used. In setup 3, a HEX cell deployment with  $R=1\,\mathrm{m}, \Delta=1, \phi_{1/2}=15^\circ$  and AMC2 is used. As shown in Fig. 22, both optical attocell systems perform better than the femtocell systems. For the attocell system with setup 2, the maximum achievable area data rate of 49 Mb/(s·m<sup>2</sup>) at a sampling frequency of 500 MHz is in a similar range of what the mmWave system can achieve. In particular, a maximum area data rate of  $469 \text{ Mb/(s} \cdot \text{m}^2)$  is achieved by the system with setup 3 with a sampling frequency of 1.26 GHz. This is about two times higher than the high performance mmWave system with a spectral efficiency of 11.25 b/(s·Hz) and a bandwidth of 2 GHz. This result highlights the huge potential of optical attocell networks.

#### IX. CONCLUSION

In this paper, the downlink performance of an optical attocell network was evaluated. In order to be able to optimally design an optical attocell system, it is important to understand how key network parameters such as cell size and network deployments affect the system performance. This is particularly important when piggy-backing the optical attocell network on existing lighting infrastructures which leaves little possibilities to optimise the network for communication. To this end, an analysis of the SINR distribution and the corresponding data rate assuming different cell deployments was performed. The analysis in this paper offers an accurate estimation of the downlink performance of an optical attocell system that is subject to a large number of parameters. This study provides detailed guidelines for appropriate configurations of these parameters. Because of the potential benefits of combining optical attocell networks with existing lighting infrastructures and due to other practical constraints, optimized regular HEX cell deployments may not always be achievable. Therefore, in this study, several other network topologies such as square and random cell deployments were also considered. In particular, an optical attocell network with PPP cell deployment was considered to closely

model a random real-world scenario where there are no underlying network planning considerations. The extensive simulation study confirms that the HEX and PPP cell deployments represent the best and the worst case performance of practical attocell deployments, respectively. The simulation results also demonstrate that the attocell networks deployed in a finite room offer better performance than the networks which are horizontally infinite because the CCI in the room edges is very low. In addition, the simulation results also imply that the MP effect due to the room internal surface reflections is minor relative to the effect of CCI. Because optical attocells can be deployed densely in a room, the optical attocell networks can typically achieve very high data rate density. In order to demonstrate this advantage, the downlink performance of optical attocell systems is compared with that achieved by RF femtocell networks and indoor mmWave systems in terms of area data rate (achievable data rate per unit area). The result showed that the optical attocell networks generally outperform the femtocell network. In particular, a high performance optical attocell network can achieve an area data rate of 469 Mb/(s·m<sup>2</sup>) which is twice that achieved by a high performance mmWave system. The mmWave system assumes a spectral efficiency of 11.25 b/(s·Hz) and uses a bandwidth of 2 GHz in a room of size  $10 \text{ m} \times 10 \text{ m}$ . The system improvement by a reduction in cell size is more pronounced in regular HEX network deployments than in random PPP network deployments. Future research will continue with the studies on the effect of handover and system uplink performance.

#### **APPENDIX**

## A. HEX Network Interference Approximation

The closed form expressions of  $\mathcal{I}_{0^{\circ}}(r_0)$  and  $\mathcal{I}_{30^{\circ}}(r_0)$  are calculated as (A.2) and (A.3), where

$$q(x,y) = ((r_0 + x)^2 + y)^{-m-3}$$
. (A.1)

### B. Derivation of (50)

The derivations start from the term with bracket in the exponent of (49). By limiting  $a \to \infty$ , this term can be calculated as (A.4), where in (a), integration by substitution is used. By using (A.4), the CF of the CCI can be found as (A.5), where in (a), the Taylor series for  $e^x$  is used.

$$\mathcal{I}_{30^{\circ}}(r_{0}) = \mathbf{1}_{\{1\}}(\Delta) \left( q \left( -\sqrt{3}\tilde{R}, h^{2} \right) + q \left( \sqrt{3}\tilde{R}, h^{2} \right) + 2q \right) \\
\times \left( -\frac{\sqrt{3}\tilde{R}}{2}, \frac{9\tilde{R}^{2}}{4} + h^{2} \right) + 2q \left( \frac{\sqrt{3}\tilde{R}}{2}, \frac{9\tilde{R}^{2}}{4} + h^{2} \right) \\
+ q \left( -2\sqrt{3}\tilde{R}, h^{2} \right) + q \left( 2\sqrt{3}\tilde{R}, h^{2} \right) \\
+ 2q \left( -\sqrt{3}\tilde{R}, 9\tilde{R}^{2} + h^{2} \right) + 2q \left( \sqrt{3}\tilde{R}, 9\tilde{R}^{2} + h^{2} \right) \right) \\
+ 2q \left( -\frac{3\sqrt{3}\tilde{R}}{2}, \frac{9\tilde{R}^{2}}{4} + h^{2} \right) + 2q \left( \frac{3\sqrt{3}\tilde{R}}{2}, \frac{9\tilde{R}^{2}}{4} + h^{2} \right) \\
+ 2q \left( 0, 9\tilde{R}^{2} + h^{2} \right), \tag{A.2}$$

$$\begin{split} \mathcal{I}_{0^{\circ}}(r_{0}) &= \mathbf{1}_{\{1\}}(\Delta) \left( 2q \left( -\frac{3\tilde{R}}{2}, \frac{3\tilde{R}^{2}}{4} + h^{2} \right) + 2q \left( \frac{3\tilde{R}}{2}, \frac{3\tilde{R}^{2}}{4} + h^{2} \right) \right. \\ &\quad + 2q \left( 0, 3\tilde{R}^{2} + h^{2} \right) + 2q \left( -3\tilde{R}, 3\tilde{R}^{2} + h^{2} \right) + 2q \\ &\quad \times \left( 3\tilde{R}, 3\tilde{R}^{2} + h^{2} \right) + 2q \left( 0, 12\tilde{R}^{2} + h^{2} \right) \right) + q \left( -3\tilde{R}, h^{2} \right) \\ &\quad + q \left( 3\tilde{R}, h^{2} \right) + 2q \left( -\frac{3\tilde{R}}{2}, \frac{27\tilde{R}^{2}}{4} + h^{2} \right) \\ &\quad + 2q \left( \frac{3\tilde{R}}{2}, \frac{27\tilde{R}^{2}}{4} + h^{2} \right) . \end{split} \tag{A.3} \\ \lim_{a \to \infty} \left( a^{2} - r_{0}^{2} - \int_{\sqrt{r_{0}^{2} + h^{2}}}^{\sqrt{a^{2} + h^{2}}} 2De^{i\omega g(D)} dD \right) \\ \stackrel{(a)}{=} \lim_{a \to \infty} \left( a^{2} - r_{0}^{2} - \left( (a^{2} + h^{2}) e^{i\omega g\left(\sqrt{a^{2} + h^{2}}\right)} - (r_{0}^{2} + h^{2}) e^{i\omega g\left(\sqrt{r_{0}^{2} + h^{2}}\right)} \right. \\ &\quad + \int_{g}^{g} \left( \sqrt{r_{0}^{2} + h^{2}} \right) \left( g^{-1}(x) \right)^{2} j \omega e^{j\omega x} dx \right) \right) \\ = \lim_{a \to \infty} \left( a^{2} \left( 1 - e^{i\omega g\left(\sqrt{a^{2} + h^{2}}\right)} \right) \right) + r_{0}^{2} \left( e^{i\omega g\left(\sqrt{r_{0}^{2} + h^{2}}\right)} - 1 \right) \\ &\quad - \lim_{a \to \infty} \left( h^{2} e^{i\omega g\left(\sqrt{a^{2} + h^{2}}\right)} \right) \right) + h^{2} e^{j\omega g\left(\sqrt{r_{0}^{2} + h^{2}}\right)} - \lim_{a \to \infty} \left( \int_{g} \left(\sqrt{r_{0}^{2} + h^{2}}\right)^{-1} \right) \right. \\ &\quad \times \left( \int_{g} \left(\sqrt{r_{0}^{2} + h^{2}}\right)^{-m-3} \left( g^{-1}(x) \right)^{2} j \omega e^{j\omega x} dx \right) \right) \\ = \left( r_{0}^{2} + h^{2} \right) \left( e^{j\omega \left(r_{0}^{2} + h^{2}\right)^{-m-3}} - 1 \right) \\ &\quad - \int_{0}^{\left(r_{0}^{2} + h^{2}\right)^{-m-3}} x^{-\frac{1}{m+3}} j \omega e^{j\omega x} dx \right) \\ &\quad + j \omega \int_{0}^{\left(r_{0}^{2} + h^{2}\right)^{-m-3}} x^{-\frac{1}{m+3}} j \omega e^{j\omega x} dx \right) \right) \\ \stackrel{(a)}{=} \exp \left( \frac{\Lambda \pi}{\Delta} \left( \left( r_{0}^{2} + h^{2} \right) \left( 1 - e^{j\omega \left(r_{0}^{2} + h^{2}\right)^{-m-3}} \right) \right. \\ &\quad + j \omega \int_{0}^{\left(r_{0}^{2} + h^{2}\right)^{-m-3}} x^{-\frac{1}{m+3}} e^{j\omega x} dx \right) \right) \\ \stackrel{(a)}{=} \exp \left( \frac{\Lambda \pi}{\Delta} \left( \left( r_{0}^{2} + h^{2} \right)^{-n+1(m+3)} \right) + j \omega \int_{0}^{\left(r_{0}^{2} + h^{2}\right)^{-m-3}} \right. \\ &\quad + \sum_{n=2}^{\infty} \frac{\left( j\omega x \right)^{n_{2}}}{n_{2}!} \cdot \frac{n_{3}(m+3) \left( r_{0}^{2} + h^{2} \right)^{1-n_{1}(m+3)}}{n_{3}(m+3) - 1} \right) \right) \right) \end{aligned}$$

$$= \exp\left(\sum_{n=1}^{\infty} \frac{(j\omega)^n}{n!} \cdot \frac{\Lambda \pi (r_0^2 + h^2)^{1-n(m+3)}}{\Delta (n(m+3)-1)}\right)$$
(A.5)

#### REFERENCES

- Cisco Visual Networking Index, "Global Mobile Data Traffic Forecast Update, 2014-2019," CISCO, White Paper, Feb. 2015.
- [2] GBI Research, "Visible light communication (VLC)—A potential solution to the global wireless spectrum shortage," Tech. Rep. GBISC017MR, 2011
- [3] V. Chandrasekhar, J. Andrews, and A. Gatherer, "Femtocell Networks: A survey," *IEEE Commun. Mag.*, vol. 46, no. 9, pp. 59–67, Sep. 2008.
- [4] H. Elgala, R. Mesleh, and H. Haas, "Indoor Optical Wireless Communication: Potential and State-of-the-Art," *IEEE Commun. Mag.*, vol. 49, no. 9, pp. 56–62, Sep. 2011.
- [5] P. Chandhar and S. Das, "Area spectral efficiency of Co-Channel deployed OFDMA femtocell networks," *IEEE Trans. Wireless Commun.*, vol. 13, no. 7, pp. 3524–3538, Jul. 2014.
- [6] H. Haas, "High-speed wireless networking using visible light," SPIE Newsroom, 2013.
- [7] S. Dimitrov and H. Haas, Principles of LED Light Communications: Towards Networked Li-Fi. Cambridge, U.K.: Cambridge Univ., 2015.
- [8] H. L. Minh, D. O'Brien, G. Faulkner, L. Zeng, K. Lee, D. Jung, Y. Oh, and E. T. Won, "100-Mb/s NRZ visible light communications using a postequalized white LED," *IEEE Photon. Technol. Lett.*, vol. 21, no. 15, pp. 1063–1065, Aug. 2009.
- [9] D. Tsonev, H. Chun, S. Rajbhandari, J. J. D. McKendry, S. Videv, E. Gu, M. Haji, S. Watson, A. E. Kelly, G. Faulkner, M. D. Dawson, H. Haas, and D. O'Brien, "A 3-Gb/s single-LED OFDM-based wireless VLC link using a gallium nitride μLED," *IEEE Photon. Technol. Lett.*, vol. 26, no. 7, pp. 637–640, Apr. 2014.
- [10] D. Tsonev, S. Videv, and H. Haas, "Unlocking spectral efficiency in intensity modulation and direct detection systems," *IEEE J. Sel. Areas Commun.*, vol. 33, no. 9, pp. 1758–1770, Sept 2015.
- [11] J. Armstrong, "OFDM for optical communications," J. Lightw. Technol., vol. 27, no. 3, pp. 189–204, Feb. 2009.
- [12] D. Tsonev and H. Haas, "Avoiding spectral efficiency loss in unipolar OFDM for optical wireless communication," in *Proc. IEEE Int. Conf. Commun.*, Sydney, Australia, Jun., 2014, pp. 3336–3341.
- [13] A. M. Khalid, G. Cossu, R. Corsini, P. Choudhury, and E. Ciaramella, "1-Gb/s transmission over a phosphorescent white LED by using rateadaptive discrete multitone modulation," *IEEE Photon. J.*, vol. 4, no. 5, pp. 1465–1473, Oct. 2012.
- [14] J. Vucic, C. Kottke, S. Nerreter, K. D. Langer, and J. W. Walewski, "513 Mbit/s visible light communications link based on DMT-modulation of a white LED," *J. Lightw. Technol.*, vol. 28, no. 24, pp. 3512–3518, Dec. 2010.
- [15] C. Chen, N. Serafimovski, and H. Haas, "Fractional frequency reuse in optical wireless cellular networks," in *Proc. Int. Symp. Personal, Indoor Mobile Radio Commun.*, London, U.K., Sep. 2013, pp. 3594–3598.
- [16] C. Chen, D. Tsonev, and H. Haas, "Joint transmission in indoor visible light communication downlink cellular networks," in *Proc. IEEE Globe-com Workshops*, Atlanta, GA, USA, Dec. 2013, pp. 1127–1132.
- [17] B. Ghimire and H. Haas, "Self-organising interference coordination in optical wireless networks," *EURASIP J. Wireless Commun. Netw.*, vol. 1, no. 131, pp. 1–15, Apr. 2012.
- [18] Z. Chen, N. Serafimovski, and H. Haas, "Angle diversity for an indoor cellular visible light communication system," in *Proc. IEEE Veh. Technol. Conf.*, Seoul, South Korea, May 2014, pp. 1–5.
- [19] Z. Chen and H. Haas, "Space division multiple access in visible light communications," in *Proc. IEEE Int. Conf. Commun.*, London, U.K., Jun. 2015, pp. 5115–5119.
- [20] L. Zeng, D. O'Brien, H. Minh, G. Faulkner, K. Lee, D. Jung, Y. Oh, and E. T. Won, "High data rate multiple input multiple output optical wireless communications using white LED lighting," *IEEE J. Sel. Areas Commun.*, vol. 27, no. 9, pp. 1654–1662, Dec. 2009.
- [21] R. Mesleh, H. Elgala, and H. Haas, "Optical spatial modulation," IEEE/OSA J. Opt. Commun. Netw., vol. 3, no. 3, pp. 234–244, Mar. 2011.
- [22] A. Azhar, T. Tran, and D. O'Brien, "A gigabit/s idoor wireless transmission using MIMO-OFDM visible-light communications," *IEEE Photon. Technol. Lett.*, vol. 25, no. 2, pp. 171–174, Jan. 15, 2013.
- [23] G. Xie, Y. Ren, H. Huang, Y. Yan, C. Bao, N. Ahmed, M. Willner, M. Lavery, M. Padgett, and A. Willner, "Analysis of aperture size for partially receiving and de-multiplexing 100-Gbit/s optical orbital

- angular momentum channels over free-space link," in *Proc. IEEE Globe-com Workshops*, Dec. 2013, pp. 1116–1120.
- [24] C. Chen, I. Muhammad, D. Tsonev, and H. Haas, "Analysis of down-link transmission in DCO-OFDM-based optical attocell networks," in *Proc. IEEE Global Commun. Conf.*, Austin, TX, USA, Dec. 2014, pp. 2072–2077.
- [25] K. Chandra, R. Venkatesha Prasad, and I. Niemegeers, "An architectural framework for 5G indoor communications," in *Proc. Int. Wireless Commun. Mobile Comput. Conf.*, Dubrovnik, Croatia, Aug. 2015, pp. 1144–1149.
- [26] M. B. Rahaim, A. M. Vegni, and T. D. C. Little, "A hybrid radio frequency and broadcast visible light communication system," in *Proc. IEEE GLOBECOM Workshops*, Dec. 2011, pp. 792–796.
- [27] (2015). Purelifi product: Li-flame. [Online]. Available: http://purelifi.com/lifi-products/li-flame/
- [28] S. Dimitrov, S. Sinanovic, and H. Haas, "Clipping noise in OFDM-based optical wireless communication systems," *IEEE Trans. Commun.*, vol. 60, no. 4, pp. 1072–1081, Apr. 2012.
- [29] J. M. Kahn and J. R. Barry, "Wireless infrared communications," *Proc. IEEE*, vol. 85, no. 2, pp. 265–298, Feb. 1997.
- [30] F. J. Lopez-Hernandez, R. Perez-Jimenez, and A. Santamara, "Ray-tracing algorithms for fast calculation of the channel impulse response on diffuse IR wireless indoor channels," *Opt. Eng.*, vol. 39, no. 10, pp. 2775–2780, 2000.
- [31] V. Jungnickel, V. Pohl, S. Nonnig, and C. von Helmolt, "A physical model of the wireless infrared communication channel," *IEEE J. Sel. Areas Commun.*, vol. 20, no. 3, pp. 631–640, Apr. 2002.
- [32] Lighting of Indoor Work Places, European Standard EN 12464-1, Jan. 2009.
- [33] J. R. Meyer-Arendt, "Radiometry and Photometry: Units and conversion factors," Appl. Opt., vol. 7, no. 10, pp. 2081–2084, Oct. 1968.
- [34] (2015, Dec.) VESTA 165 mm Recessed LED Downlighter. [Online]. Available: http://www.istl.com/vesta.php
- Available: http://www.istr.com/vesta.pnp [35] (2014, Aug.). 64 W LED panel. [Online]. Available: http://wellmaxled.com/portfolio/64-w-led-panel-light/
- [36] F. R. Gfeller and U. Bapst, "Wireless in-house data communication via diffuse infrared radiation," *Proc. IEEE*, vol. 67, no. 11, pp. 1474–1486, Nov. 1979.
- [37] J. Andrews, F. Baccelli, and R. Ganti, "A tractable approach to coverage and rate in cellular networks," *IEEE Trans. Commun.*, vol. 59, no. 11, pp. 3122–3134, Nov. 2011.
- [38] H. Elgala, R. Mesleh, and H. Haas, "Non-linearity effects and predistortion in optical OFDM wireless transmission using LEDs," *Inderscience Int. J. Ultra Wideband Commun. Syst.*, vol. 1, no. 2, pp. 143–150, 2009.
- [39] D. Tsonev, S. Sinanovic, and H. Haas, "Complete modeling of nonlinear distortion in OFDM-based optical wireless communication," *J. Lightw. Technol.*, vol. 31, no. 18, pp. 3064–3076, Sep. 15, 2013.
- [40] B. Almeroth, A. Fehske, G. Fettweis, and E. Zimmermann, "Analytical interference models for the downlink of a cellular mobile network," in *Proc. IEEE Globcom Workshops*, Houston, TS, USA, Dec. 5–9, 2011, pp. 739–743.
- [41] E. Sousa and J. Silvester, "Optimum transmission ranges in a direct-sequence spread-spectrum multihop packet radio network," *IEEE J. Sel. Areas Commun.*, vol. 8, no. 5, pp. 762–771, Jun. 1990.
- [42] J. Bowers and L. Newton, "Expansion of probability density functions as a sum of gamma densities with applications in risk theory," *Trans. Soc. Actuaries*, vol. 18, no. 52, pp. 125–147, 1966.
- [43] M. Haenggi, "On distances in uniformly random networks," *IEEE Trans. Inf. Theory*, vol. 51, no. 10, pp. 3584–3586, Oct. 2005.
- [44] F. Xiong, Digital Modulation Techniques, 2nd ed. Norwood, MA, USA: Artech House, 2006.
- [45] H. Burchardt, S. Sinanović, Z. Bharucha, and H. Haas, "Distributed and autonomous resource and power allocation for wireless networks," *IEEE Trans. Commun.*, vol. 61, no. 7, pp. 2758–2771, Aug. 2013.
- [46] D. Stoyan, W. S. Kendall, and J. Mecke, Stochastic Geometry and Its Applications, 2nd ed. Hoboken, NJ, USA: Wiley, 1995.
- [47] C. Hansen, "WiGiG: Multi-Gigabit wireless communications in the 60 GHz Band," *IEEE Wireless Commun.*, vol. 18, no. 6, pp. 6–7, Dec. 2011.
- [48] H.-S. Jo, P. Xia, and J. Andrews, "Downlink femtocell networks: Open or closed?" in *Proc. IEEE Int. Conf. Commun.*, Kyoto, Japan, Jun., 2011, pp. 1–5.
- [49] W. C. Cheung, T. Quek, and M. Kountouris, "Throughput optimization, spectrum allocation, and access control in two-tier femtocell networks," *IEEE J. Sel. Areas Commun.*, vol. 30, no. 3, pp. 561–574, Apr. 2012.

- [50] D. Muirhead, M. A. Imran, and K. Arshad, "Insights and approaches for low-complexity 5G small-cell base-station design for indoor dense networks," *IEEE Access*, vol. 3, pp. 1562–1572, 2015.
- [51] C. Yiu and S. Singh, "Empirical capacity of mmWave WLANS," *IEEE J. Sel. Areas Commun.*, vol. 27, no. 8, pp. 1479–1487, Oct. 2009.

Cheng Chen (S'14) received the B.Eng. degree in electronic and electrical engineering (first class hons.) from the University of Strathclyde, Glasgow, U.K., in 2011, and the M.Sc. degree in communications and signal processing from the Imperial College, London, U.K., in 2012. He is currently working toward the Ph.D. degree in electrical engineering from the University of Edinburgh, Edinburgh, U.K.. His research focus include the visible light communication networking and interference mitigation.

Dushyantha A. Basnayaka (S'11–M'12) received the B.Sc. Eng. degree (first class hons.) from the University of Peradeniya, Peradeniya, Sri Lanka, in 2006, and the Ph.D. degree in electrical engineering from the University of Canterbury, Christchurch, New Zealand, in 2012. From 2006 to 2009, he was with MillenniumIT (a member company of the London Stock Exchange Group). From 2009 to 2012, he was with the Communication Research Group, the University of Canterbury. He is currently with the Institute for Digital Communications, the University of Edinburgh, Edinburgh, U.K. He is a holder of one U.S. patent. His current research interests include massive multiple-input multiple-output, spatial modulation, interference mitigation techniques for cellular wireless systems, coordinated multipoint systems, and visible light communication systems. He received the University of Canterbury International Doctoral Scholarship for his Doctoral Studies and the Best Paper Award at the Spring 2015 IEEE Vehicular Technology Conference (IEEE VTC-Spring 2015).

Harald Haas (S'98-AM'00-M'03) received the Ph.D. degree from the University of Edinburgh, Edinburgh, U.K., in 2001. He is currently the Chair of Mobile Communications at the University of Edinburgh, and is the Cofounder and Chief Scientific Officer of pureLiFi Ltd. and the Director of the LiFi Research and Development Center at the University of Edinburgh. His main research interests include optical wireless communications, hybrid optical wireless and RF communications, spatial modulation, and interference coordination in wireless networks. He first introduced and coined spatial modulation and LiFi. LiFi was listed among the 50 best inventions in TIME Magazine 2011. He was an Invited Speaker at TED Global 2011, and his talk: "Wireless Data from Every Light Bulb" has been watched online more than 2.2 million times. He gave the second TED Global lecture in 2015 on the use of solar cells as LiFi data detectors and energy harvesters which was viewed online more than 1 million times. He holds 31 patents and has more than 30 pending patent applications. He has published 300 conference and journal papers including a paper in Science. He coauthors a book entitled: "Principles of LED Light Communications Towards Networked Li-Fi" (Cambridge, U.K.: Cambridge Univ. Press, 2015). He was a corecipient of recent Best Paper Awards at the IEEE Vehicular Technology Conference (VTC-Fall) in Las Vegas in 2013, and VTC-Spring in Glasgow in 2015. He was a corecipient of the EURASIP Best Paper Award for the Journal on Wireless Communications and Networking in 2015, and a corecipient of the Jack Neubauer Memorial Award of the IEEE Vehicular Technology Society. In 2012, he received the prestigious Established Career Fellowship from the Engineering and Physical Sciences Research Council (EPSRC) within Information and Communications Technology in the U.K. He received the Tam Dalyell Prize 2013 awarded by the University of Edinburgh for excellence in engaging the public with science. In 2014, he was selected by EPSRC as one of ten Recognizing Inspirational Scientists and Engineers Leaders in the U.K.